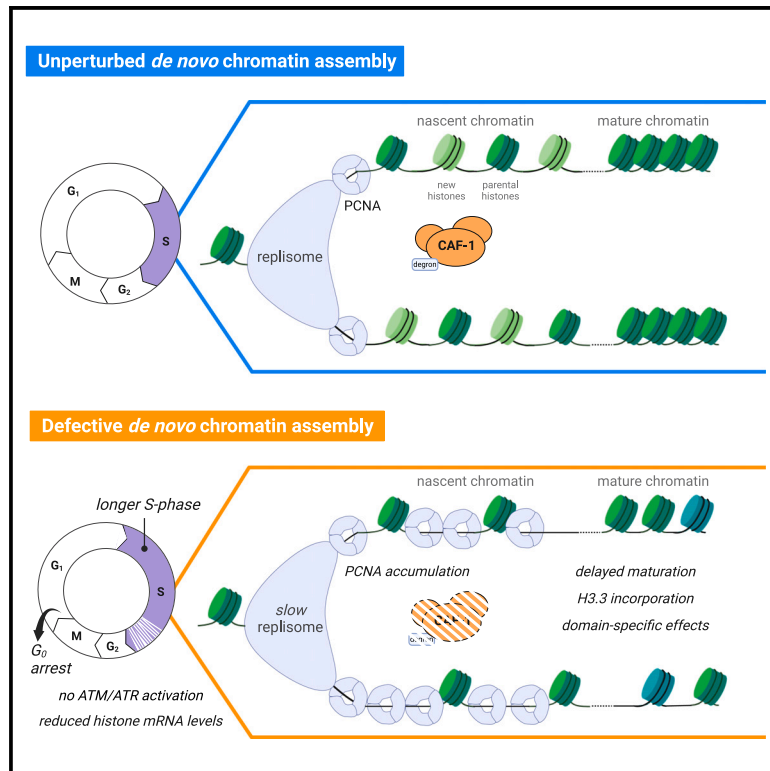**Article**

Acute multi-level response to defective *de novo* chromatin assembly in S-phase

Graphical abstract

Authors

Jan Dreyer, Giulia Ricci,
Jeroen van den Berg, ...,
Sabrina L. Spencer,
Alexander van Oudenaarden,
Francesca Mattiroli

Correspondence

f.mattiroli@hubrecht.eu

In brief

Dreyer et al. show the broad and rapid impact that acute inhibition of chromatin formation in S-phase has on DNA replication, chromatin stability, and cell-cycle progression. This study sheds light on the molecular mechanisms underlying epigenome inheritance during the cell cycle.

Highlights

- The histone chaperone CAF-1 sustains DNA replication speed in single cells

- CAF-1 loss alters histone repertoire and delays chromatin maturation

- H3K9me3 and H3K27me3 regions respond differently to acute CAF-1 depletion

- Impaired S-phase chromatin assembly triggers an immediate response and a G0 arrest

CellPress

Molecular Cell

Article

Acute multi-level response to defective *de novo* chromatin assembly in S-phase

Jan Dreyer,[1,12] Giulia Ricci,[1,12] Jeroen van den Berg,[1,2,12] Vivek Bhardwaj,[1,2] Janina Funk,[1] Claire Armstrong,[3,4] Vincent van Batenburg,[1,2] Chance Sine,[3,4] Michael A. VanInsberghe,[1,2] Rinskje B. Tjeerdsma,[5] Richard Marsman,[1] Imke K. Mandemaker,[1] Simone di Sanzo,[6] Juliette Costantini,[1] Stefano G. Manzo,[2,7,8] Alva Biran,[9] Claire Burny,[6] Marcel A.T.M. van Vugt,[5] Moritz Völker-Albert,[6] Anja Groth,[9,10,11] Sabrina L. Spencer,[3,4] Alexander van Oudenaarden,[1,2] and Francesca Mattiroli[1,13,*]

[1]Hubrecht Institute, KNAW & University Medical Center Utrecht, Uppsalalaan 8, 3584 CT Utrecht, the Netherlands
[2]Oncode Institute, Utrecht, the Netherlands
[3]Department of Biochemistry, University of Colorado Boulder, Boulder, CO 80303, USA
[4]BioFrontiers Institute, University of Colorado Boulder, Boulder, CO 80303, USA
[5]Department of Medical Oncology, University of Groningen, University Medical Center Groningen, Groningen, the Netherlands
[6]MOLEQLAR Analytics GmbH, Rosenheimer Street 141 h, 81671 Munich, Germany
[7]Division of Gene Regulation, Netherlands Cancer Institute, Plesmanlaan 121, 1066 CX Amsterdam, the Netherlands
[8]Department of Biosciences, Università degli Studi di Milano, Via Celoria 26, 20133 Milan, Italy
[9]Novo Nordisk Foundation Center for Protein Research, University of Copenhagen, Copenhagen 2200, Denmark
[10]Biotech Research & Innovation Centre, University of Copenhagen, Copenhagen 2200, Denmark
[11]Department of Cellular and Molecular Medicine, University of Copenhagen, Copenhagen 2200, Denmark
[12]These authors contributed equally
[13]Lead contact
*Correspondence: f.mattiroli@hubrecht.eu
https://doi.org/10.1016/j.molcel.2024.10.023

SUMMARY

Long-term perturbation of *de novo* chromatin assembly during DNA replication has profound effects on epigenome maintenance and cell fate. The early mechanistic origin of these defects is unknown. Here, we combine acute degradation of chromatin assembly factor 1 (CAF-1), a key player in *de novo* chromatin assembly, with single-cell genomics, quantitative proteomics, and live microscopy to uncover these initiating mechanisms in human cells. CAF-1 loss immediately slows down DNA replication speed and renders nascent DNA hyper-accessible. A rapid cellular response, distinct from canonical DNA damage signaling, is triggered and lowers histone mRNAs. In turn, histone variants' usage and their modifications are altered, limiting transcriptional fidelity and delaying chromatin maturation within a single S-phase. This multi-level response induces a p53-dependent cell-cycle arrest after mitosis. Our work reveals the immediate consequences of defective *de novo* chromatin assembly during DNA replication, indicating how at later times the epigenome and cell fate can be altered.

INTRODUCTION

During every cell cycle, the entire genome must be accurately replicated. This process occurs in the context of chromatin, a highly organized DNA-protein complex that encodes epigenetic information essential for cell identity and survival.[1] Chromatin is organized in repetitive structural units called nucleosomes, which are composed of two copies of the histones H2A, H2B, H3, and H4, wrapped by 150 bp of DNA. Histones and their different variants provide a platform for post-translational modifications (PTMs) that locally control chromatin organization and DNA accessibility.[2] Because these features regulate gene transcription and affect cell identity, faithful inheritance of chromatin during cell division is essential to safeguard the fate of daughter cells.[3–5]

The mechanisms that control the inheritance of chromatin are tightly coupled to the cell cycle.[3–8] As DNA is copied, histones on parental DNA are recycled with their PTMs onto the two replicated strands to maintain local epigenetic information. Concomitantly, *de novo* deposition of newly synthesized histones safeguards nucleosome density on nascent DNA. These new histones are highly acetylated (H4K5ac and H4K12ac)[9,10] but lack local epigenetic PTMs known to affect gene expression. These PTMs are therefore re-established after DNA replication through a process called chromatin maturation. Chromatin maturation mechanisms differ along chromosomes, depending on the local environment,[11–14] with heterochromatic histone PTMs accumulating with slower kinetics than the ones associated with active transcription.[12] This is despite heterochromatin-related factors

being recruited rapidly on replicated DNA.[14] In addition, to enable the rapid supply of histones, S-phase cells coordinate their production with DNA replication.[6,8,15–18] Long-term depletion of chromatin assembly during DNA replication can translate into cell-cycle defects.[19–23] Thus, S-phase chromatin dynamics safeguard epigenome stability and cell fate by orchestrating a complex network of diverse processes.

De novo chromatin assembly during DNA replication is a central part of this network.[1,6–8,21,22,24–26] This process is coordinated by the histone chaperone chromatin assembly factor 1 (CAF-1).[27] CAF-1 is a heterotrimeric complex (composed of CHAF1A, CHAF1B, and RBBP4) that receives newly synthesized H3-H4 from ASF1 and deposits them onto replicated DNA upon recruitment by the essential replication clamp PCNA.[9,27–40] CAF-1 also interacts with heterochromatin protein 1 (HP1) to control replication of constitutive H3K9me3-marked heterochromatin.[41–44] Previous studies using knockout (KO) or RNAi-mediated depletion of CAF-1 have demonstrated its functions in safeguarding DNA replication and epigenome stability over multiple cell cycles and its essential roles in organismal development and cell fate determination.[23–26,37,45–52] The immediate mechanisms that link CAF-1 to DNA replication and chromatin organization within a single cell cycle remain unclear.

Recent technological developments allow the acute depletion of proteins on a minute-to-hour timescale in cells.[53,54] Combined with single-cell genomics, quantitative proteomics, and live-imaging technologies, these enable us to monitor immediate changes in chromatin organization, DNA replication, and cell-cycle progression, revealing the early mechanisms associated with *de novo* chromatin assembly during DNA replication.

RESULTS

Acute depletion of CAF-1 curtails DNA replication speed in single cells

To investigate the effects of acute depletion of CAF-1, we generated human RPE-1 (retinal pigment epithelial 1) cell lines with a bi-allelic endogenous knockin of an N-terminal FKBP12[F36V] tag[53] on the largest subunit of CAF-1, named CHAF1A/p150 (referred to as degron-CHAF1A). This system enables rapid degradation of CHAF1A as early as 10 min after addition of the dTAG[V]-1 ligand (referred to as dTAG, Figures 1A and S1A), without affecting the levels of the upstream histone chaperone ASF1 (Figure 1A). Because CHAF1A directly controls interactions with histones, DNA replication proteins, and epigenetic factors,[29,34,55–58] our newly generated cell lines enable us to acutely inactivate CAF-1 and its key functionalities with high temporal resolution.

CAF-1 acts during DNA replication and its depletion affects 5-ethynyl-2′-deoxyuridine (EdU) incorporation levels (Figure S1B) as previously observed,[25,34,42] indicating that it influences DNA synthesis. Therefore, we first set out to determine how DNA replication is affected by acute depletion of CAF-1. To this end, we applied single-cell EdU-sequencing (scEdU-seq) on degron-CHAF1A cells to monitor location and speed of replication forks genome-wide with single-cell resolution[59] (Figure 1B). Acute CAF-1 depletion (i.e., 10 min before EdU labeling) leads to a decrease in replication speed genome-wide throughout S-phase (Figure 1C). This effect is strongest in late S-phase

when heterochromatic regions are replicated[60] (Figure 1C). These observations were independently confirmed using DNA fiber assays, which also show a marked reduction in DNA replication speed upon CAF-1 depletion (2 h), which is most severe in late S-phase cells (Figures 1D and S1C).

Interestingly, there are no global alterations in DNA replication timing upon CAF-1 loss (Figures 1E, S1D, and S1E). Moreover, we measure a similar number of replication forks per cell (Figures S1F and S1G), and a similar percentage of cells displayed robust DNA replication profiles across S-phase (Figure S1H). Therefore, we conclude that acute depletion of CAF-1 slows down the speed of replication forks without halting DNA replication. Interestingly, we also observe an increase in the standard deviation of the speed of replication forks within single cells (Figure 1F), indicating that fork speed becomes more heterogeneous. Although this could be due to different CAF-1 depletion levels among single cells, it is interesting that we find a stronger effect in late S-phase cells (Figure S1I). The effect of CAF-1 loss on replication speed is not exacerbated over time, as removal of CAF-1 for longer periods (2 h before EdU labeling) results in a comparable slowdown (Figure S1J) with no effects on replication timing (Figure S1K). Together, these data demonstrate that CAF-1 sustains DNA replication speed.

CAF-1 depletion prolongs S-phase without triggering ATM or ATR activation

Next, we asked how the slowdown of replication forks affected S-phase progression. We monitored cell-cycle progression by live microscopy at a single-cell level using a CDK2 activity sensor.[61] By aligning single cells according to the time of dTAG or DMSO addition relative to their last anaphase, we evaluated the effect of CAF-1 loss dependent on the different cell-cycle phases. Strikingly, acute CAF-1 loss in early or late S-phase causes an immediate plateau in CDK2 activity (Figures 2A, 2B, S2A, and S2B). Conversely, cells that lose CAF-1 in G1 phase do not respond immediately: they ramp up CDK2 activity normally until they enter S-phase (Figures 2C and S2C). Moreover, cells where CAF-1 is depleted in G2 do not change CDK2 activity until their daughter cells reach the next S-phase (Figures 2D and S2D). These data demonstrate that CAF-1 depletion is rapidly sensed only during S-phase, dampening CDK2 activity build-up. Importantly, in line with DNA replication not stopping, we do not observe an S-phase arrest. The dampening of CDK2 activity is sustained until entry into mitosis, which we observe in all cells depleted of CAF-1 (Figures S2A–S2D). These data were confirmed by flow cytometry analysis, showing that CAF-1-depleted cells spend more time in S-phase, but not in G2/M, after release from CDK4/6 inhibition[62] (Figure S2E). Thus, CAF-1 loss slows down DNA replication speed, thereby prolonging S-phase and extending cell-cycle duration.

To investigate the mechanism of DNA replication slowdown, we tested whether cell-cycle checkpoints are activated upon acute CAF-1 depletion. Previous studies using long-term (i.e., 48–72 h) depletion or mutations of CAF-1 in fly, human, or mouse cells reported checkpoint activation,[20–23] while others reported no effects on either DNA damage checkpoints or cell-cycle progression.[25,42,48] Acute depletion of CAF-1 in our system did not cause an increase in phosphorylation of CHK1 (Ser317 or
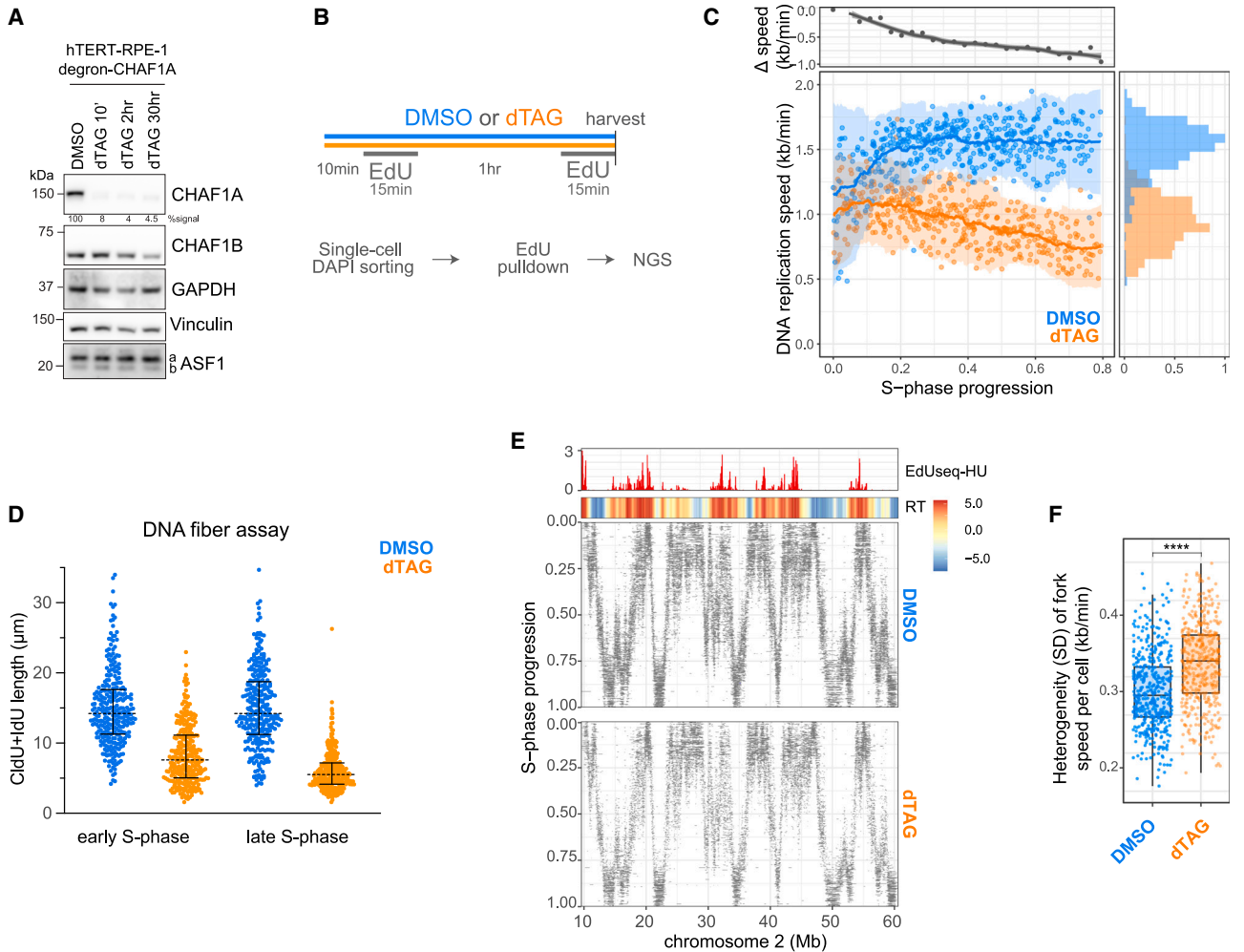
Figure 1. CAF-1 sustains DNA replication speed in single cells

(A) Western blot analysis of RIPA-extracted hTERT RPE-1 degron-CHAF1A cells treated with DMSO or dTAG for indicated time periods. The mean percentage of CHAF1A signal was calculated on at least three independent replicates.

(B) Schematic representation of the treatment and sample preparation for scEdU-seq experiments.

(C) DNA replication speed over S-phase in degron-CHAF1A treated with DMSO (blue) or dTAG (orange, 500 nM). Difference in DNA replication speeds between DMSO and dTAG in kb/min (y axis) over S-phase progression (x axis, top left), marginal normalized density (x axis) of DNA replication speed in kb/min (y axis) colored for DMSO- (blue) or dTAG-treated cells (orange, bottom-right). Each dot represents a single cell.

(D) DNA fiber length analysis using DNA spread analysis from the indicated cell population labeled with CldU and IdU.

(E) Heatmap showing scEdU-seq maximum normalized log counts for DMSO-treated and dTAG-treated degron-CHAF1A cells ordered according to S-phase progression (y axis) and binned per 40 kb bins (x axis) for a 50-Mb region of chromosome 2. Top: heatmap showing $\log_2$-fold ratio of early to late Repli-seq indicating replication timing (top) and bar graph showing EdU-seq-HU, to mark replication origins (bottom).

(F) Boxplots showing heterogeneity of fork speed within single cells expressed as the standard deviation of DNA replication speeds (kb/min, y axis) from degron-CHAF1A cells treated with DMSO or dTAG (x axis). Adjusted *p* values were determined by pairwise t test and corrected Bonferroni multiple testing correction.

Ser345), CHK2 (Thr68), H2AX (Ser139), CDK1(Tyr15), or RPA (Ser4/8) (Figures 2E, 2F, and S2F). Moreover, inhibition of the DNA damage kinases ATR, ATM, or Wee1 kinases did not rescue the reduction of EdU intensity seen upon CAF-1 depletion (Figure 2G). These data indicate that acute CAF-1 depletion does not trigger an ATM or ATR response.

Nonetheless, in line with previous reports on players in the new histone supply pathway,[25,63,64] we did observe an accumulation of PCNA on chromatin after 2 h of CAF-1 depletion, without significant depletion of the available soluble PCNA

pool (Figure 2H). We also observed increased levels of the PCNA unloading complex ATAD5 on chromatin (Figure 2H), indicating that PCNA accumulation is not due to unavailability of the unloader. Thus, PCNA dynamics are rapidly altered upon CAF-1 degradation. Remarkably, this accumulation is not observed after low-dose aphidicolin treatment, which also slows down replication speed (Figures S2G and S2H). Hence, PCNA accumulation is not a general phenotype of slower DNA replication speeds but may represent a specific marker of defective S-phase chromatin assembly.
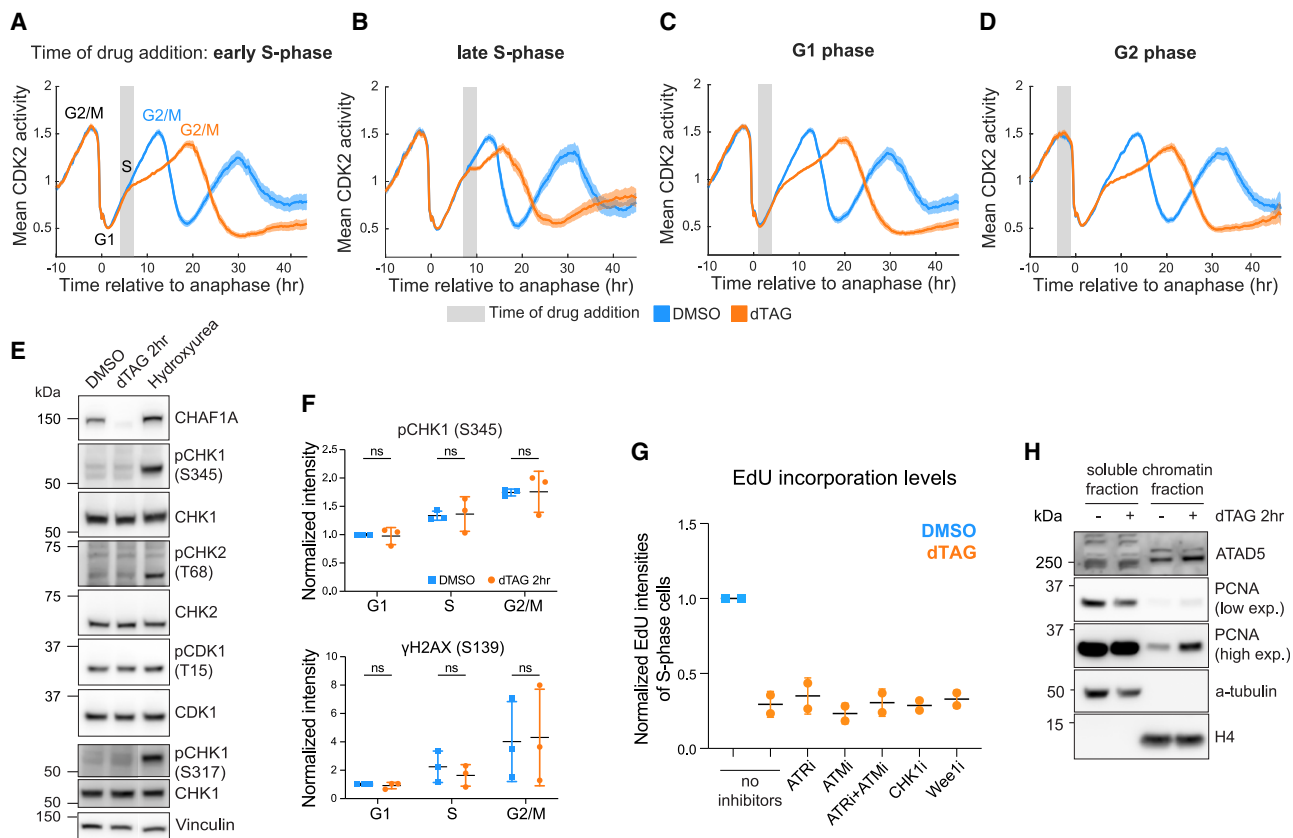
Figure 2. Acute CAF-1 depletion prolongs S-phase without triggering ATM or ATR activation

(A–D) Mean signal of CDK2 activity sensor aligned computationally to the time of anaphase. Cells included in the different analyses experienced the start of DMSO (blue) or dTAG (orange, 1 μM) treatment relative to their last anaphase in indicated cell-cycle phases.

(E) Western blot analysis of RIPA-extracted degron-CHAF1A cells treated for 2 h with DMSO, dTAG, or HU (hydroxyurea) (10 mM) probed with indicated antibodies.

(F) Flow cytometry analysis for pCHK1 (S345) and γH2AX (S139) intensities for indicated cell-cycle phases in degron-CHAF1A cells treated for 2 h with DMSO (blue) or dTAG (orange). Error bars represent SD as a result of unpaired, parametric t tests (ns, non-significant).

(G) Corrected EdU intensities for DMSO or dTAG (2 h) degron-CHAF1A S-phase cells treated with indicated inhibitors.

(H) Western blot of soluble and chromatin fraction of RPE-1 degron-CHAF1A cells treated with DMSO or dTAG (2 h) probed with indicated antibodies.

S-phase cells acutely respond to CAF-1 depletion

To understand the immediate cellular response to acute CAF-1 depletion, we sought to analyze the transcriptional effects upon defective *de novo* chromatin assembly in the different cell-cycle phases. To this end, we performed single-cell RNA sequencing using VASA-seq (scVASA-seq), which enables sequencing of all RNA, including non-polyadenylated genes (e.g., histone genes).[65] This allowed us to analyze changes in the transcriptional profile of short-term CAF-1-depleted cells (2 h) per cell-cycle phase. In addition to control treatment with dimethyl sulfoxide (DMSO), we also used long-term CAF-1-depleted cells (30 h), which are expected to display a strong and diverse transcriptional response.[49,55] To analyze the VASA-seq data, we used Leiden clustering to uncover cell clusters (Figures 3A and S3A), followed by a uniform manifold approximation and projection (UMAP) visualization of cell states per condition (Figures 3B, S3B, and S3C).[65] CAF-1-depleted cells behave distinctly from DMSO-treated and wild-type (WT) cells. Particularly, upon short-term CAF-1 depletion (2 h), only

S-phase cells are affected (gray dotted line, compare clusters 3 and 7) (Figures 3A, 3C, and S3A). This confirms that CAF-1 loss is rapidly sensed in S-phase and alters cell-cycle states. Upon longer CAF-1 depletion (30 h), more cell-cycle phases are affected, with the rise of unique G0/G1 and S/G2 populations (see clusters 6 and 9, respectively) (Figures 3A, 3D, and S3A–S3C). These analyses support the notion that inactivation of CAF-1 leads to immediate transcriptional effects only during S-phase. Conversely, prolonged CAF-1 loss more broadly affects the cell cycle. Thus, CAF-1 is closely wired into S-phase regulatory mechanisms.

CAF-1 depletion affects histone mRNA levels in S-phase

Because acute CAF-1 depletion specifically affects S-phase cells, we investigated the differentially expressed genes in this condition. We found 50 significantly upregulated and 61 significantly downregulated genes (Figure S3D). 42 of these 61 downregulated genes are histone transcripts, indicating a global reduction in histone mRNAs (Figures 3E, S3D, and
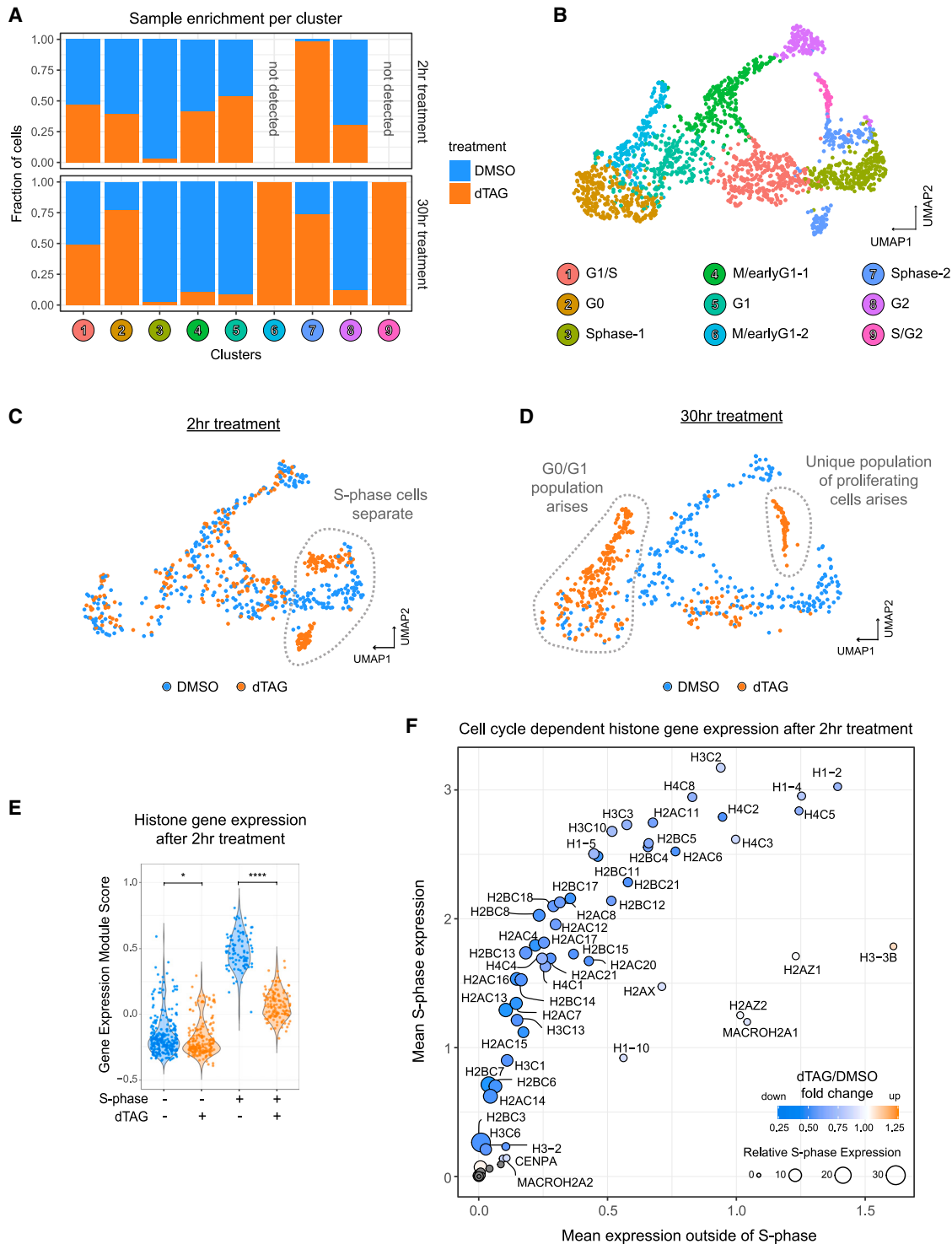
Figure 3. CAF-1 depletion lowers histone mRNAs in S-phase

(A) Stacked bar graph displaying the normalized contribution of each experimental condition to each Leiden cluster (x axis).

(B) UMAP plot obtained from total gene-wise RNA counts of sequenced cells analyzed with Seurat, colored by cycle stages identified by unsupervised clustering, and characterized with marker genes for cell-cycle progression shown in Figure S3B. Each dot represents a single cell.

(C and D) UMAPs determined using total RNA counts per gene illustrating cells treated for 2 h (C) or 30 h (D) with DMSO or dTAG. Differences are highlighted in gray.

(legend continued on next page)

S3E; Table S1), also confirmed by RNA fluorescence *in situ* hybridization (FISH) of H4.2 transcripts in S-phase cells (Figure S3F). This phenotype was dominated by the specific down-regulation of replicative histone mRNAs, such as H3.1/2 and H4 (Figures 3F and S3G), whose expression is mostly restricted to S-phase and whose translation relies on stem-loop-dependent mechanisms. In contrast, mRNA levels of non-replicative histone variants, expressed throughout the cell cycle and translated by polyadenylation-dependent mechanisms, such as H3.3, H2AZ, and macroH2A, did not decrease upon CAF-1 depletion (Figures 3F and S3H). Analysis of H2AX transcripts confirms these findings, with a decrease in reads only upstream of the stem-loop region, and no changes for reads of the 3′ untranslated region (UTR) region[66] (Figures S3I and S3J). These data indicate that CAF-1 depletion triggers an acute response that lowers replicative histone mRNA levels in S-phase, which does not affect histone mRNAs that rely on canonical polyadenylation mechanisms. This is in line with previous observations linking replicative histone mRNA stability to the supply of new histones.[8,23,25,67–71]

CAF-1 loss leads to histone imbalance and delays chromatin maturation within a single S-phase

To directly measure how these effects impact histone composition and PTMs in chromatin, we used a SILAC-based quantitative mass spectrometry approach, which measures newly synthesized (i.e., new) and parental (i.e., old) histone variants and their PTMs (Figure 4A, S4A, and S4B).[72] We quantified the relative abundance of histones H3 and H4 after a single S-phase upon CAF-1 depletion (Figure 4B). In line with a reduction in histone mRNAs and the reduction in soluble histone proteins upon CAF-1 depletion, we observe a decrease in newly synthesized replicative histones H3.1/2 (Figures 4B and S4C). Conversely, we find an increase in newly synthesized H3.3 protein (Figure 4B), also confirmed by western blot (Figure 4C). As 98% of cellular histones are incorporated into chromatin,[73] our data suggest that, upon CAF-1 loss, newly replicated chromatin is enriched in the non-replicative H3.3 variant, which likely compensates for the decrease in canonical H3.1/2 histones. This was also observed upon RNAi depletion of CAF-1.[74,75] We show that this is rapid, as it occurs as early as in the first S-phase when CAF-1 is depleted. We find similar trends in newly synthesized non-replicative H2A variant proteins increasing compared with canonical H2A upon CAF-1 loss (Figure S4D), with a less prominent effect compared with H3.3 on total protein levels (Figures 4C and S4E).

We analyzed histone PTMs on the unique peptide that distinguishes the tail of H3.1/2 or H3.3. This peptide encompasses residues K27 and K36, which are established targets of epigenetic marks,[76] where H3K27 is methylated in transcriptionally

silenced regions and H3K36 in active domains. We found significant changes in the relative abundance of H3K27 and H3K36 methylation status in old and new H3.1/2 and H3.3 (Figures 4D and S4F), with a distinct effect seen on newly synthesized H3.3 peptides. In control DMSO conditions, new H3.3 shows a higher percentage of H3K36 methylation compared with H3K27 methylation. Upon dTAG treatment, new H3.3 peptides reversed this distribution, displaying a higher percentage of H3K27 methylation, resembling the distribution of these marks on H3.1/2 (Figure 4D). Thus, upon CAF-1 depletion, newly synthesized H3.3 mimics the H3.1/2 distribution of H3K27 and H3K36 methylation status, implying that in cells lacking CAF-1, newly synthesized H3.3 is incorporated in genomic regions where, in unperturbed conditions, H3.1/2 resides.

Next, we analyzed global changes in other histone H3 and H4 PTMs. Several histone PTMs are significantly affected by CAF-1 depletion, most notably H3K4me1, H3K18ac, acetylation of the H4 N-terminal tail (amino acid [aa] 4–17), and the heterochromatic mark H3K9me3 (Figures 4E, S4G, and S4H; Table S2). However, the most pronounced effects were observed for the methylation status of H4K20 (Figures 4E and 4F). H4K20 methylation functions as a timer for histone age, from their synthesis in early S-phase (H4K20me0) to their later maturation on chromatin starting from late G2 (H4K20me1/2).[12,77–80] We found a relative increase in H4K20me0 and a corresponding relative decrease in H4K20me2 on both new and old histones (Figure 4F). This suggests that chromatin is "younger" (i.e., less mature) after a single S-phase in the absence of CAF-1. Interestingly, its effect involves not only the pool of newly synthesized histones but also the parental (i.e., old) histones in chromatin, indicating that *de novo* chromatin assembly during S-phase has the potential to alter epigenetic states within a single S-phase.

Together, these data show that CAF-1 loss within a single S-phase alters the protein levels of histones H3 and H4, with consequences for global chromatin composition at the end of S-phase.

CAF-1 assembles nascent chromatin genome-wide

To understand the mechanisms that lead to these global changes in chromatin composition, we set out to monitor how chromatin organization is affected by CAF-1 depletion during S-phase. To this end, we applied repli-ATAC-seq, which measures chromatin accessibility specifically at replicated regions.[81] In combination with acute CAF-1 depletion, this approach allows us to directly measure the role of CAF-1 in assembling replicated chromatin along the genome with high temporal resolution. Using this technique, we analyzed (1) nascent chromatin to observe CAF-1-dependent effects during DNA replication, (2) mature chromatin to measure the effects of prolonged CAF-1 loss during and after DNA replication, and (3) post-replication chromatin to

---

(E) Violin plot of the single-cell expression analysis for all histone genes using ModuleScore function from Seurat for 2 h DMSO- or dTAG-treated degron-CHAF1A cells split by non-S-phase and S-phase clusters. S-phase clusters are 3 and 7. Adjusted *p* values were obtained by pairwise t test followed by Bonferroni multiple testing correction. See Table S1.

(F) Analysis of CAF-1-dependent expression of all histone genes. In this scatterplot, each histone gene is represented by a dot, which is colored by the fold change in expression in acute CAF-1 depletion (2 h, dTAG/DMSO). Gray denotes genes not detected in DMSO or dTAG samples. Their size indicates the relative S-phase expression (S-phase/outside of S-phase expression), defined as a fold enrichment per histone gene. The x axis represents the mean expression of each histone gene outside of S-phase and the y axis represents the mean expression of each histone gene in S-phase.
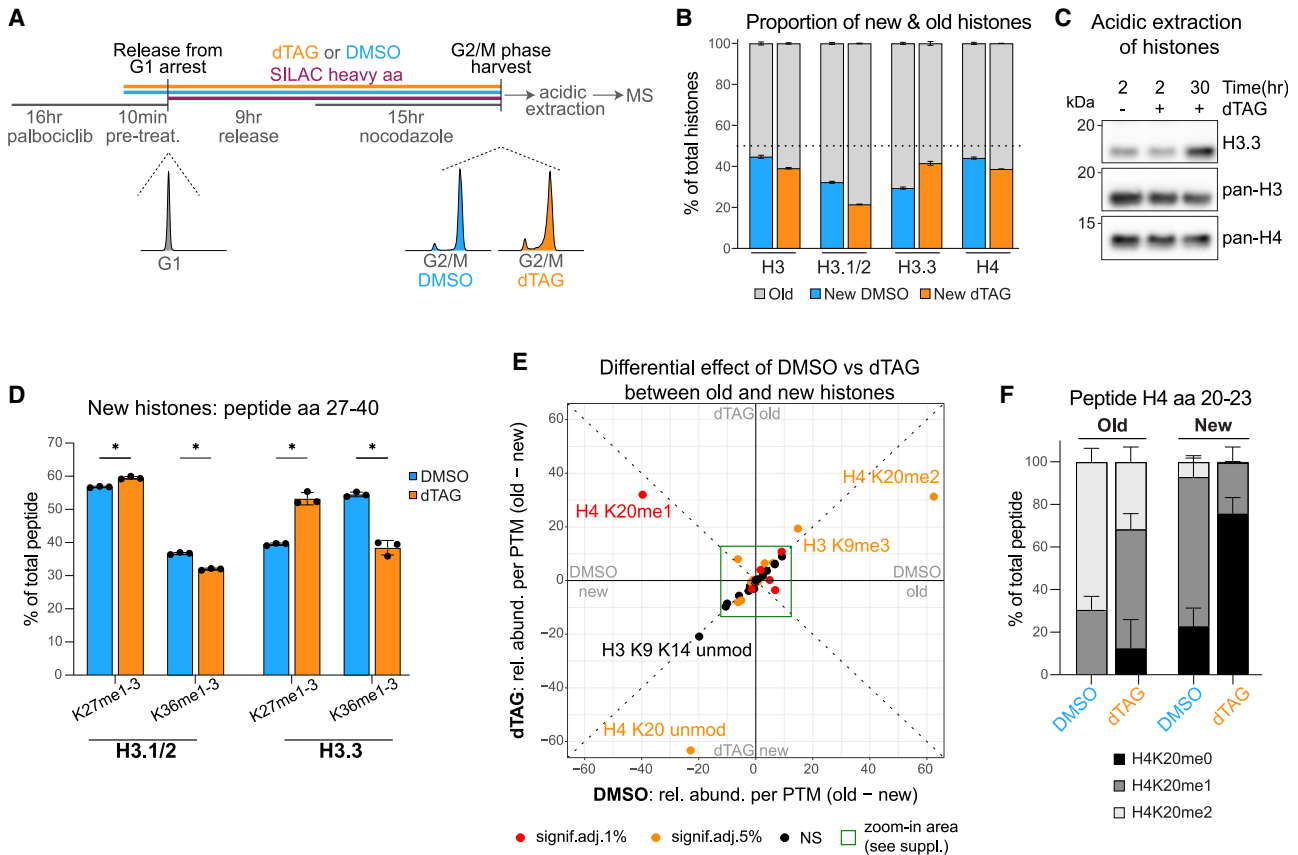
CellPress
OPEN ACCESS

Figure 4. CAF-1 loss leads to histone imbalance and globally affects chromatin maturation within a single S-phase

(A) SILAC-mass spectrometry set up for analysis of old and new histones, their PTMs and variants of cells that underwent exactly one full S-phase after the start of DMSO/dTAG treatment. DAPI FACS profiles of the different conditions are shown.

(B) Cumulative bar plots of the proportion of old and new histones in DMSO and dTAG. The horizontal dotted line is set at 50%.

(C) Western blot of acidic extractions of degron-CHAF1A cells (clone 8) treated with DMSO or dTAG for indicated times.

(D) Quantification of new H3.1/2 and H3.3 peptides (amino acids 27–40). The height of the bar plots represents the relative abundances of mono-, di-, and tri-methylation of K27 or K36 that were summed up.

(E) Scatterplot of the differential effect of DMSO (x axis) vs. dTAG (y axis) between old and new histones. Colors encode significance levels (p value) after Benjamini-Hochberg adjustment. A zoom-in is available in Figure S4G.

(F) Quantification of the H4K20-anchored PTMs' relative abundance on old and new H4 peptides 20–23, associated with DMSO or dTAG treatment.

(B, D, and F) Quantification of histones and their PTMs of degron-CHAF1A cells (clone 8) treated as described in (A). Percentages are relative to the total intensity of related peptides and averaged across $n = 3$ biological replicates. Error bars represent SD, asterisks represent p values as *$p < 0.05$, **$p < 0.01$, ***$p < 0.001$, ****$p < 0.0001$ as a result of unpaired, parametric t tests. See Table S2.

observe the role of CAF-1 after DNA replication (Figures 5A and S5A). EdU-labeled S2 *Drosophila* chromatin was used as spike-in and to control for changes in EdU incorporation (Figure S5B).

In nascent chromatin, CAF-1 depletion leads to an increase in sub-nucleosomal fragments and to a decrease in mono- and di-nucleosomal fragments (Figures 5B and 5C), indicating loss of nucleosomes on nascent DNA. In contrast, in mature or post-replication chromatin, CAF-1 depletion has milder effects, namely an increase in linker length between nucleosomes (i.e., mono- and di-nucleosomal peaks shift to higher sizes) (Figures 5B and 5C). These data show that CAF-1 significantly alters chromatin on nascent DNA, as expected.[29,42]

To quantify the genome-wide effects of CAF-1 on chromatin accessibility, we plotted the distribution of the fold change of the repli-ATAC signal in dTAG over DMSO samples in 15-kb

bins. In nascent chromatin, 99% of the genome displays a positive fold-change enrichment (Figures 5D, 5E, and S5C), demonstrating that acute CAF-1 depletion results in a dramatic gain of accessibility on newly replicated DNA genome-wide. This effect decreases over time after DNA replication, with an intermediate increase in accessibility after 2 h of chromatin maturation (mature 2 h, Figure 5E) and a near-complete recovery of accessibility after 15 h (mature 15 h, Figures 5E and S5C). These data indicate that after DNA replication during chromatin maturation, CAF-1-independent backup mechanisms facilitate nucleosome assembly, as previously proposed.[74] Post-replication removal of CAF-1 results in a limited increase in genome-wide chromatin accessibility (Figures 5D and 5E), confirming that the main role of CAF-1 is during DNA replication. Moreover, we performed ATAC-seq after a 2-h depletion of CAF-1 to assess the chromatin
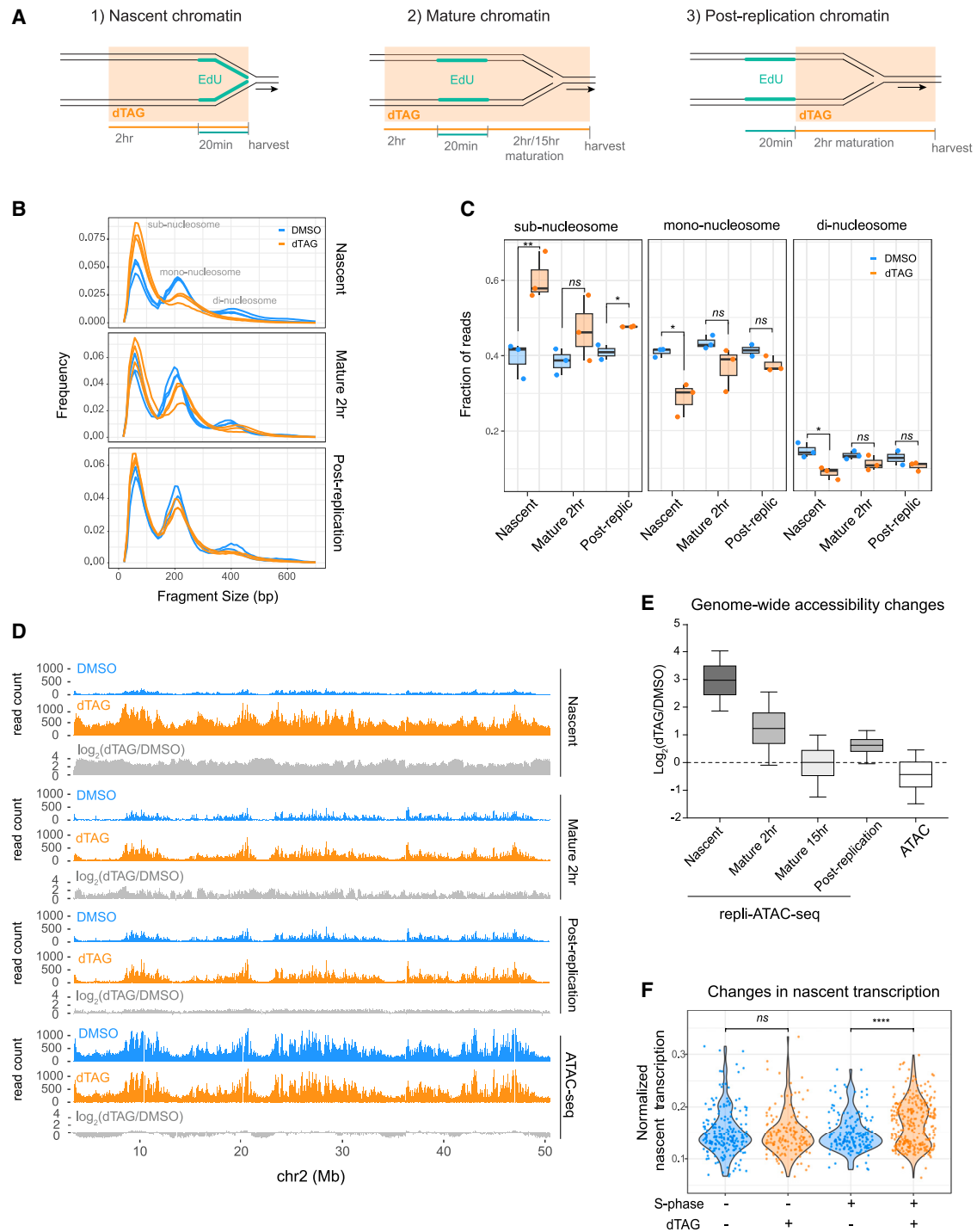
Figure 5. CAF-1 controls chromatin assembly in S-phase

(A) Schematics of repli-ATAC-seq conditions.

(B) Fragment size frequency of repli-ATAC-seq samples for nascent, mature 2 h, and post-replication chromatin from three independent experiments.

(C) Boxplot quantification of reads within the sub-nucleosomal (<150 bp), mono-nucleosomal (150–300 bp), and di-nucleosomal (300–450 bp) size range relative to the total amount of DNA fragments. *p* values were calculated using binomial test.

(D) Spike-in normalized signal of nascent, mature, and post-replication repli-ATAC-seq samples and ATAC-seq sample over a selected region of about 50 Mb on chromosome 2. In blue DMSO control samples, in orange dTAG-treated samples, in gray log$_2$ fold-change quantification of dTAG over DMSO signal.

Molecular Cell
Article

CellPress
OPEN ACCESS

accessibility changes at steady-state level and detected no global alterations (Figures 5D and 5E). Similar results were obtained when analyzing the parental non-replicated regions from repli-ATAC-seq samples, which also showed no global alteration in chromatin accessibility (Figures S5C and S5D). These data demonstrate that CAF-1 controls chromatin assembly during DNA replication at a genome-wide scale, with no major roles in nucleosome assembly outside of DNA replication.

CAF-1 loss alters transcriptional fidelity in S-phase

Next, we investigated whether the opening of nascent chromatin upon acute CAF-1 loss alters nascent transcription. To this end, we analyzed the ratio of unspliced over spliced RNA molecules in our scRNA-seq data after short-term CAF-1 depletion. We found an increase in nascent transcription specifically in S-phase cells (Figure 5F). Thus, defective *de novo* chromatin assembly during DNA replication leads to loss of transcriptional fidelity during S-phase, suggesting that proper chromatin assembly affects the transcriptional state of genes behind replication forks. To see whether this was due to changes in the accessibility of annotated promoters and genic and intergenic (e.g., enhancers) regions, we analyzed our repli-ATAC-seq datasets and found that accessibility of these regions is altered in nascent chromatin, in line with the global accessibility changes observed earlier (Figure S5E). This supports the notion that the opening of nascent chromatin observed upon CAF-1 depletion promotes a loss of transcriptional fidelity, as also seen recently in *Saccharomyces cerevisiae* CAF-1 KO strains.[82,83]

Taken together, CAF-1 acts globally to assemble chromatin during DNA replication across the entire genome. Via this function, CAF-1 safeguards transcriptional fidelity of the replicated genome. These data indicate that backup nucleosome assembly pathways may promote chromatin compaction[74] but that they are not sufficient to restore functional chromatin organization. This is also supported by the global changes we observe in histone variants and PTMs after a single S-phase in cells depleted of CAF-1 (Figure 4).

Acute CAF-1 loss differentially affects constitutive and facultative heterochromatin

Previous CAF-1 RNAi or KO studies have shown loss of heterochromatin stability after multi-day treatments.[26,37,41–44,55,84] In our proteomic data, CAF-1 loss has a significant effect on constitutive heterochromatin H3K9me3 modification, where this mark increases in old histones and decreases in new ones upon CAF-1 depletion (Figures 4E and S4E). Moreover, the facultative Polycomb-associated H3K27me3 mark significantly increases on all histones, with strongest effects on the new H3.3 variant (Figures 4D, S4C, and S4D). To understand how CAF-1 contributes to these changes and the reported phenotypes, we monitored chromatin accessibility within these regions in our different repli-ATAC-seq datasets. In nascent chromatin, both heterochromatic regions showed a significant increase in accessibility compared with the rest of the genome during DNA replication when CAF-1 is depleted (Figures 6A, 6B, and S6A). However, the CAF-1-dependent opening of H3K9me3-marked regions is more dramatic than in H3K27me3 domains (Figures 6A and S6A, nascent samples). These data indicate that the initial compaction of both heterochromatic regions during DNA replication is particularly susceptible to CAF-1 loss.

After DNA replication, constitutive H3K9me3 heterochromatin starts to compact during chromatin maturation (2 h), independently of CAF-1. This compaction stabilizes at longer chromatin maturation times (15 h), reaching the accessibility levels observed in the ATAC-seq sample (Figures 6A–6C and S6A–S6C). These observations indicate that, although H3K9me3 heterochromatin opens up more dramatically during DNA replication upon CAF-1 depletion, other mechanisms rapidly compensate for CAF-1 loss after DNA replication to promote its compaction. This compaction appears exacerbated by the absence of CAF-1, also at steady-state conditions (Figure 6D).

In contrast, the less drastic chromatin accessibility defects in H3K27me3 domains observed in nascent chromatin persist during chromatin maturation (Figure 6E). Thus, CAF-1-independent chromatin maturation mechanisms are unable to fully rescue chromatin compaction defects at H3K27me3 domains, at least up to 15 h after DNA replication. Strikingly, the opening of these regions is not observed outside of DNA replication, such as at steady-state conditions (i.e., ATAC-seq after 2 h dTAG treatment) or in the post-replication or unbound (non-EdU-labeled) samples (Figure 6E). These controls indicate that the defects in compaction of H3K27me3 regions are strictly dependent on CAF-1 function during DNA replication.

Taken together, H3K9me3- and H3K27me3-marked heterochromatin are highly susceptible to CAF-1 loss during DNA replication, displaying increased chromatin accessibility defects on nascent DNA. Interestingly, compaction of H3K9me3 chromatin can be recovered post-replication by CAF-1-independent mechanisms, while H3K27me3 regions persist in a hyper-accessible state for over 15 h after DNA replication. Moreover, CAF-1 loss may increase constitutive heterochromatin compaction at a steady-state level, raising the possibility of local CAF-1 activities in these regions beyond DNA replication.

Prolonged CAF-1 depletion results in loss of transcriptional fidelity in facultative heterochromatin

To understand the functional consequences of these changes in chromatin accessibility, we monitored the distribution of the heterochromatic histone PTMs along the genome after CAF-1 loss. Neither H3K27me3 nor H3K9me3 displays significant changes after long-term (15 or 30 h) CAF-1 depletion, as seen in ChIC-seq[85] (Figures S6D and S6E). Thus, domain-level distributions of these histone marks do not change within a single S-phase. However, when we analyzed whether these regions are

(E) Boxplot quantifying accessibility signal changes of dTAG over DMSO genome-wide (15-kb bins) in different repli-ATAC-seq conditions and ATAC-seq (2 h dTAG).
(F) Violin plots of single-cell nascent transcription quantification as determined by the number of unique spliced (mature) total RNA reads divided by the number of unique unspliced (nascent) total RNA, as produced by the Velocyto program for CHAF1A cells treated for 2 h with DMSO and dTAG split by non-S-phase and S-phase clusters. Adjusted *p* values were obtained by pairwise t test followed by Bonferroni multiple testing correction.
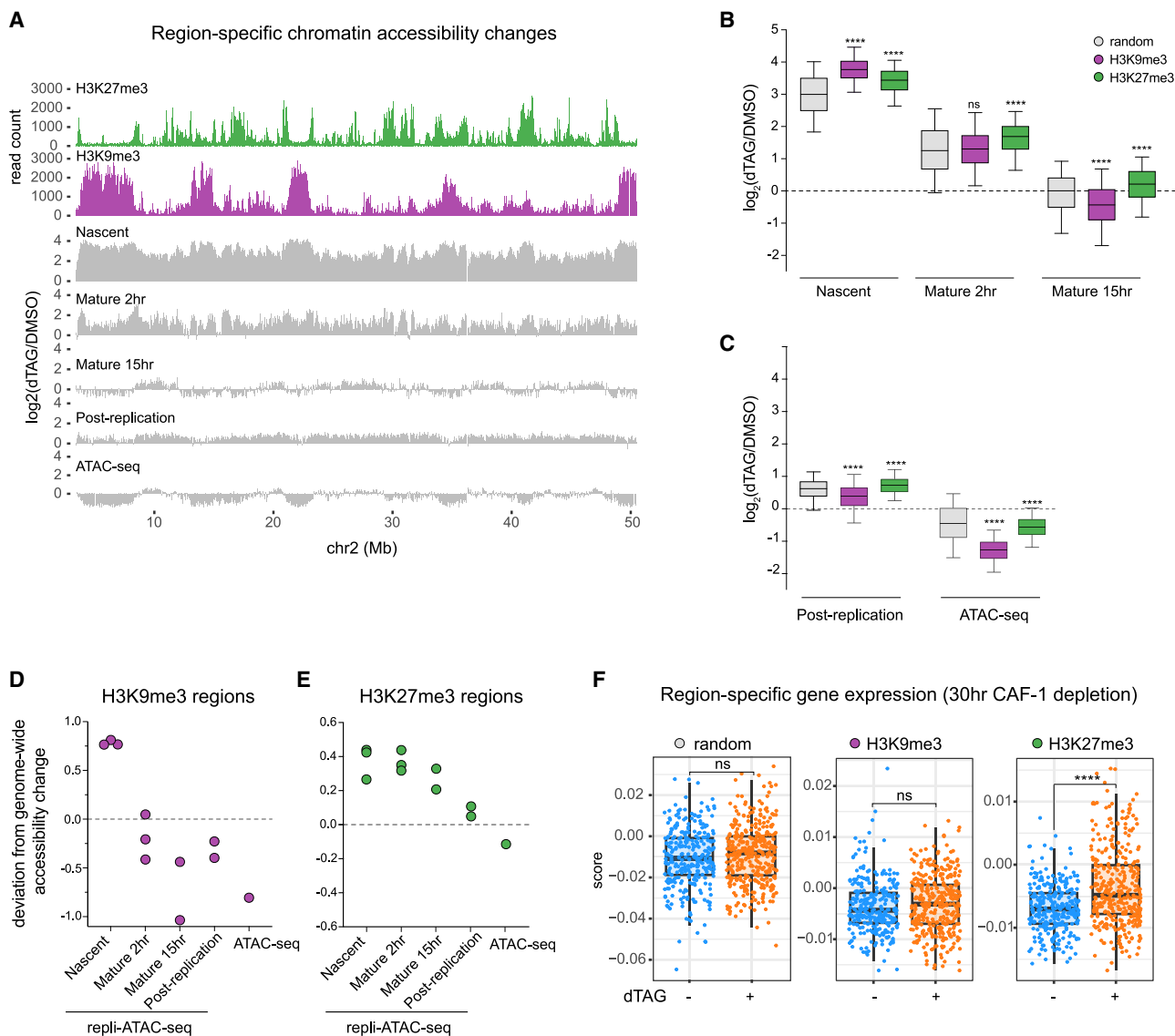
Figure 6. Acute CAF-1 loss differentially affects constitutive and facultative heterochromatin

(A) Genomic tracks of ChIC-seq signal for H3K9me3 (purple) and H3K27me3 (green) in DMSO-treated cells. In gray: tracks showing changes in accessibility following CAF1 depletion for repli-ATAC and ATAC-seq experiments, over 50 Mb loci on chromosome 2.

(B and C) Boxplots of changes in accessibility signal, upon CAF-1 removal, per region, in nascent, mature (2 h or 15 h), post-replication repli-ATAC-seq samples, and in ATAC-seq (2 h). Each boxplot represents 1,000 bins, either randomly selected genome-wide (gray) or selected by the highest ChIC-seq signal for H3K9me3 (purple) and H3K27me3 (green) regions. One-way ANOVA test was performed to determine statistically significant differences between each genomic region within each sample. Correlation analysis over the whole genome is shown in Figure S6A.

(D and E) Quantification of the differences between the median of the randomly selected bins and the median of the heterochromatic regions (H3K9me3 in purple, H3K27me3 in green) from (B) and (C). Wilcoxon test was used to extract the median for each genomic region within sample and used to quantify its deviation from the genome-wide accessibility signal for H3K9me3 and H3K27me3 regions in all repli-ATAC-seq samples and ATAC sample.

(F) Boxplots of single-cell expression analysis using ModuleScore function from Seurat. Cells were treated with 30 h of DMSO (blue) or dTAG (orange). Panels show module expression levels for 250 random genes in the genome (left) or in 250 genes with the highest accessibility scores in H3K9me3 regions (middle) and 250 genes with the highest accessibility scores in H3K27me3 regions (right). See Table S1.

transcriptionally de-regulated in our scRNA-seq data, we found that transcripts originating from H3K27me3 regions are slightly, but significantly, increased after 30 h of CAF-1 depletion (Figure 6F; Table S1). This effect is specific to H3K27me3 domains, as a randomized gene set or transcripts from H3K9me3 regions

do not show such an increase in transcript levels (Figure 6F; Table S1). These data show that sustained accessibility of H3K27me3 domains after DNA replication upon CAF-1 depletion can alter their transcriptional state, whereas CAF-1-independent mechanisms safeguard the integrity of H3K9me3 regions, at
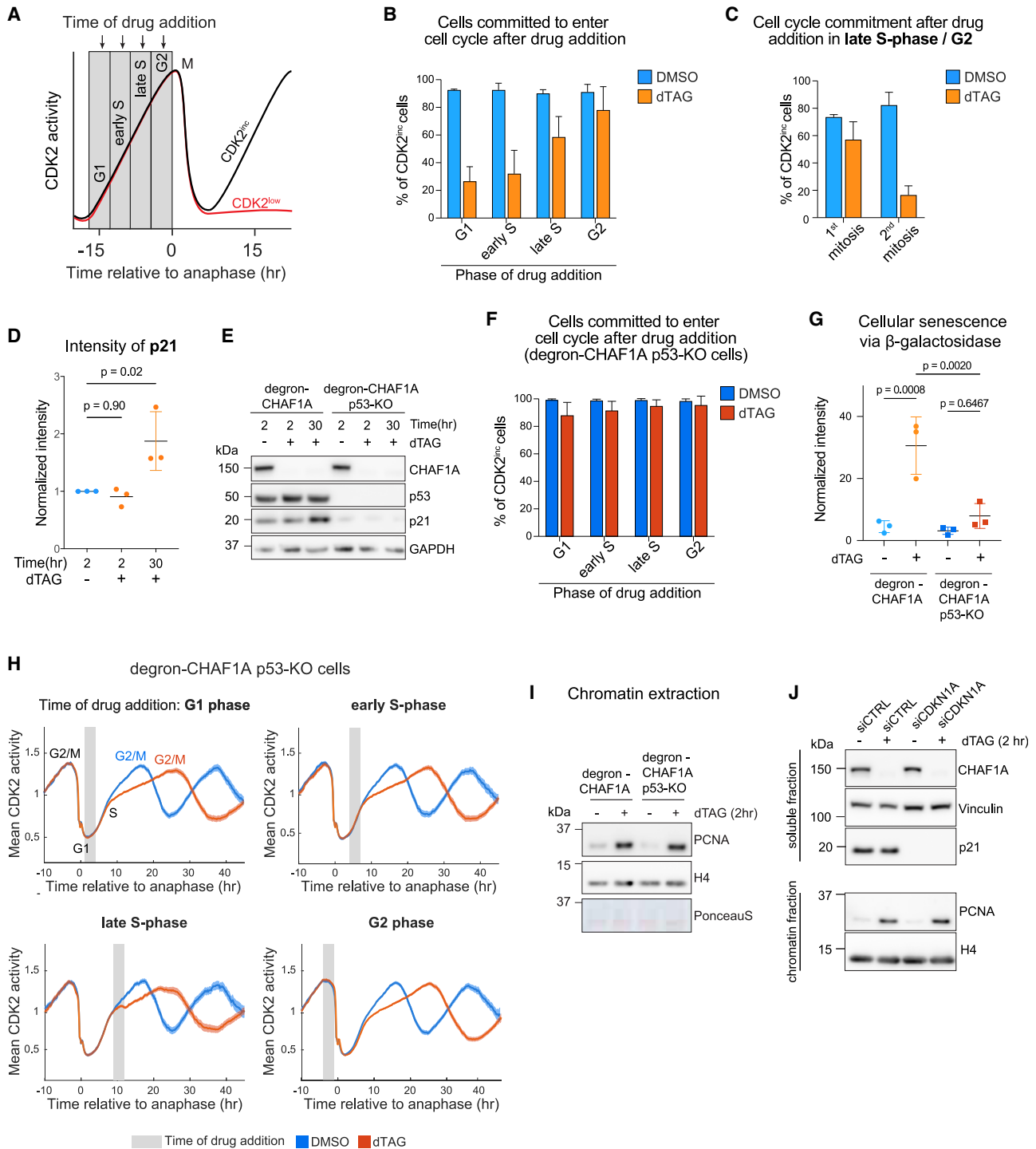
Figure 7. Defective de novo chromatin assembly in S-phase leads to a G0 arrest in daughter cells

(A) Schematic representation of live microscopy data (see Figures 2A–2D). CDK2-increasing cells (CDK2^{inc}) and CDK2-low cells (CDK2^{low}) are used to calculate the percentage of cells that are committed to enter the cell cycle (CDK^{inc}) vs. the percentage of cells that enter G0 arrest (CDK^{low}).

(B) Quantification of CDK2^{inc} cells of experiments shown in Figures 2A–2D. Blue: DMSO, orange: dTAG. Error bars represent the standard deviation.

(C) Quantification of CDK2^{inc} cells of experiments shown in Figures 2B and 2D, separated by first and second mitosis after treatment. Blue: DMSO, orange: dTAG. Error bars represent the standard deviation.

(D) Flow cytometry analysis of p21 levels in degron-CHAF1A cells at indicated time points.

(E) Western blot of RIPA-extracted cell lysates of degron-CHAF1A and degron-CHAF1A p53-KO cells at indicated time points.

(legend continued on next page)

least within the first 30 h. Moreover, our data suggest that the loss of transcriptional fidelity may result from changes beyond histone PTM distribution at a domain-wide level. In fact, our mass spectrometry experiments showed that newly synthesized H3.3 acquires H3K27me1-3 modifications upon CAF-1 loss (Figure 4D), suggesting the deposition of this histone variant within these domains. Thus, histone H3.3 variants' incorporation could in part explain the functional changes in H3K27me3 regions.

Defective *de novo* chromatin assembly in S-phase activates p53 and leads to a G0 arrest in daughter cells

CAF-1 has pleiotropic effects in S-phase cells within a few hours. To understand how these effects impinge on cell proliferation, we used our time-lapse imaging data of the CDK2 activity sensor (Figures 2A–2D) and quantified the number of cells committed to cell-cycle re-entry after CAF-1 depletion. We noticed that acute CAF-1 depletion reduced the number of cells committed to enter a new cell cycle after mitosis (Figures 7A and 7B). This effect was stronger for cells that lost CAF-1 earlier in the cell cycle (i.e., G1 and early S-phase) compared with cells losing CAF-1 in late S or G2 phase (Figure 7B). Moreover, cells treated in late S or G2-phase underwent two mitoses before withdrawing from the cell cycle (i.e., G0 arrest) (Figure 7C). Thus, the time spent after CAF-1 depletion in the cell cycle inversely correlates to the commitment of daughter cells to enter a new cell cycle. This suggests that cells need to undergo a full S-phase with defective *de novo* chromatin assembly before entering a G0 arrest. A G0 arrest was confirmed by flow cytometry (Figure S7A) and by single-cell transcriptomic data after 30 h CAF-1 depletion showing an increase in a G0 transcriptional state[86] (Figures S7B and S7C; Table S1). Thus, CAF-1 depletion precludes re-entry into a new cell cycle after experiencing a perturbed S-phase.

Cell-cycle arrest is often associated with p53-dependent mechanisms, and previous works linked CAF-1 to the p53-p21 axis.[20–22] In line with this, p21 levels increased after 30 h of CAF-1 depletion (Figure 7D), whereas phosphorylation of the DNA damage checkpoint kinase CHK1 remained undetected (Figure S7D). Moreover, we find a transcriptional signature linked to a p53-dependent stress response related to low histone levels[87] as early as after 2 h of CAF-1 depletion (Figure S7E; Table S1). Thus, p53 is engaged rapidly during defective *de novo* chromatin assembly, without detectable activation of canonical checkpoints. To directly address the role of p53, we generated an RPE-1 TP53 KO degron-CHAF1A line (degron-CHAF1A p53-KO) (Figure 7E). Live-imaging of the CDK2 sensor in this cell line shows that p53-KO cells do not arrest in G0 after one S-phase with defective *de novo* chromatin assembly (Figure 7F). Moreover, p53-KO prevents p21 stabilization (Figure 7E)

and entry into senescence upon extended CAF-1 depletion (Figure 7G). Therefore, p53 controls the G0 cell-cycle arrest upon CAF-1 loss. Remarkably, CAF-1-depleted p53-KO cells still display longer S-phase progression (Figure 7H), lower EdU incorporation levels (Figure S7F), and proliferation defects (Figure S7G), indicating that DNA replication defects are independent of p53. Moreover, CAF-1 depletion still led to PCNA accumulation on chromatin in p53-KO cells (Figure 7I) and in p21-depleted cells (Figure 7J), indicating that PCNA accumulation is not dependent on p53 or p21.

DISCUSSION

A close interplay between DNA replication and chromatin assembly

Our work shows that CAF-1 closely controls DNA replication speed at a genome-wide level. Thus, we support a direct link between *de novo* chromatin assembly on nascent DNA and the speed of replication forks, as previously suggested.[25,42] In line with this work, PCNA plays a role in this mechanism, accumulating on chromatin together with its unloader ATAD5. Interestingly, depletion of ATAD5 phenocopies the acute loss of CAF-1, also leading to slower replication speed and an S-phase delay.[63,88] Thus, PCNA levels on chromatin control replisome progression, with CAF-1 regulating these levels. As we find plenty of PCNA in the soluble pool, we conclude that small changes in PCNA levels on chromatin can cause or be a consequence of impaired DNA replication. Because PCNA accumulates also upon perturbation of other components of the *de novo* histone deposition pathway,[25] but not when DNA is slowed down by chemical perturbations (i.e., aphidicolin), we favor a model where nucleosome assembly contributes to PCNA unloading.[25,88] Other possible mechanisms may involve the direct interaction between CAF-1 and PCNA[32,33,36] and the binding competition to PCNA with DNA polymerases.[34] In addition to PCNA-dependent effects, chromatin itself may hold nascent DNA strands in a conformation that favors optimal replisome progression. To support this hypothesis, we find a positive correlation between the severity of nascent chromatin opening and DNA replication slowdown in heterochromatic regions.

We show that within just 2 h of depletion of *de novo* chromatin assembly, S-phase cells trigger a shutdown program for replicative histone mRNAs, likely involving post-transcriptional histone mRNA processing.[67,70] In contrast, recent work showed that 2-day RNAi depletion of CHAF1B did not affect histone mRNAs.[67] This suggests that either CHAF1A and CHAF1B do not have fully overlapping functions within S-phase or that the timing and the single-cell approach of our study provide

---

(F) Quantification of CDK2^{inc} cells of experiments shown in Figure 7H in degron-CHAF1A p53-KO cells. Dark blue: DMSO, red: dTAG. Error bars represent the standard deviation.

(G) Flow cytometry analysis of cellular senescence via B-galactosidase hydrolysis. Cells were treated for 7 days with DMSO or dTAG. The intensity of CellEvent Senescence Green per cell was normalized to an unstained control. *p* values were calculated using Student's t test.

(H) Mean signal of CDK2 activity sensor in degron-CHAF1A p53-KO cells aligned computationally to the time of anaphase. Cells included in the different analyses experienced the start of DMSO (dark blue) or dTAG (red, 1 μM) treatment relative to their last anaphase in indicated cell-cycle phases.

(I) Western blot of chromatin fraction of degron-CHAF1A cells treated with DMSO or dTAG (2 h) probed with indicated antibodies.

(J) Western blot of soluble and chromatin fraction. Degron-CHAF1A cells were treated with siCTRL and siCDKN1A (p21 RNAi) for 48 h before DMSO or dTAG (2 h) were added. Membranes were probed with indicated antibodies.

Molecular Cell
Article

increased resolution into this effect. In any case, our data support a model where the state of newly replicated DNA has a direct influence on replisome progression genome-wide and that this is rapidly sensed at the cellular level.

Epigenome instability upon CAF-1 loss: Different effects in constitutive and facultative heterochromatin

We show that acute CAF-1 depletion affects the global composition and accessibility of chromatin within a single S-phase, in line with its chromatin assembly function.[9,21,27] Although domain-scale distributions of heterochromatic PTMs are not affected, we observe alterations in histone variant usage as well as in chromatin compaction, its maturation, and transcriptional fidelity within hours of CAF-1 loss. These phenotypes likely cause the epigenetic instability and plasticity previously observed upon long-term CAF-1 depletion.[26,37,46,48–50,84] Both H3K9me3 and H3K27me3 heterochromatin become hyperaccessible during DNA replication upon CAF-1 depletion. Yet, these two regions differentially recover from this excessive opening after DNA replication, indicating that local mechanisms have an impact on the consequences of defective de novo chromatin assembly during DNA replication.

Facultative H3K27me3 heterochromatin is particularly susceptible to CAF-1 loss, as it remains more open than the rest of the genome for several hours after DNA replication. Moreover, we find a small but significant increase in transcription of genes within these regions, suggesting a functional link between these domains and CAF-1 loss during their replication. A link had also been previously reported during in vitro cell differentiation[37] and development in plants.[84] We propose that this likely requires replication through these domains. In Drosophila, Polycomb domains are sensitive to histone levels,[89] supporting a fragility of these regions when histones are limiting. Mechanistically, our data point to an increase of H3.3 within these domains, after a single S-phase with limiting CAF-1 levels.[74,75] Whether H3.3 directly affects Polycomb domains by preventing local chromatin organization and modifications,[90–93] or whether H3.3 accumulation is only one aspect of a global histone imbalance that ultimately disrupts the stability of these domains, remains to be investigated.

Constitutive H3K9me3 heterochromatin regions display the most severe opening during DNA replication upon CAF-1 depletion. These regions do not open up outside of DNA replication, implicating a role for CAF-1 in controlling accessibility of these regions during DNA replication.[42] However, H3K9me3 domains efficiently recompact after DNA replication in a CAF-1-independent manner, and we find that they are also more compacted at steady-state levels, upon CAF-1 depletion. This suggests that CAF-1 loss may affect H3K9me3 heterochromatin outside the context of DNA replication. The nature of this replication-independent effect of CAF-1 remains unclear, with possible local contributions to the slowdown of replication forks in late S-phase. It will be important to shed light on these mechanisms, such as the involvement of the CAF-1-HP1a interaction[41–44] or the de novo deposition of H3.3K9me3.[94,95] As we did not observe significant changes in H3K9me3 marks at the domain-level upon CAF-1 loss, we expect that higher resolution mapping of histone PTMs and their replication-coupled dynamics[96–99] will

be important approaches to disentangle the mechanistic link between CAF-1 and heterochromatin stability.

Toward understanding the link between CAF-1 and cell fate decisions

Our data show that cells that have experienced a full S-phase with limiting CAF-1 levels do not continue cycling after mitosis. This underlines the essentiality of this complex,[21,26,45–47] raising important questions on the mechanisms at the core of cell fate changes upon long-term CAF-1 depletion.[37,48–50,100,101] Cells need to escape cell-cycle arrest to support those changes. This will require rapid adaptations. The loss of epigenome stability that we observe already within a single S-phase likely facilitates the plasticity required to acquire these adaptations and to evade cell-cycle arrest, with the contribution of environmental cues.[102] Understanding the nature of the adaptations that allow the bypassing of cell-cycle arrest is of great interest. These will reveal both the mechanisms that underpin CAF-1-mediated cell-cycle control and the ones that foster cell fate determination.

Limitations of the study

We estimate that about 5% of CHAF1A is still present in our cells; therefore, the phenotypes we report could be partially mitigated by these residual CAF-1 levels. However, our phenotypes are dramatic and rapid, showing the power of acute degradation and its combination with genomics and imaging. The molecular mechanisms that link the diverse phenotypes we observe remain elusive. Future work is required to understand which effects are directly controlled by CAF-1 itself, which ones are indirectly linked to its functions, and how. Moreover, CAF-1 may have activities outside S-phase, and how these further tune the phenotypes of CAF-1-depleted cells remains to be studied. Finally, although RPE-1 cells represent a well-characterized and genetically stable system for mechanistic cell biological studies, the use of other cell lines, such as mouse embryonic stem cells, can provide critical information on the link between de novo chromatin assembly and cell fate.

RESOURCE AVAILABILITY

Lead contact

Further information and requests for resources and reagents should be directed to and will be fulfilled by the lead contact, Francesca Mattiroli (f.mattiroli@hubrecht.eu).

Materials availability

Materials generated in this study will be made available.

Data and code availability

- The proteomics data are available at PRIDE: PXD050618. The repli-ATAC-seq, scVASA-seq, and scEdU-seq data are available at GEO: GSE262518.
- All original code has been deposited at GitHub and Zenodo and is publicly available at https://doi.org/10.5281/zenodo.13918157 as of the date of publication. R scripts can be found as supplemental information. Raw western blot and imaging files have been deposited to Mendeley Data: https://doi.org/10.17632/n9h2mj7dbg.1.
- Any additional information required to reanalyze the data reported in this paper is available from the lead contact upon request.

AUTHOR CONTRIBUTIONS

F.M., J.D., and G.R. conceived the project; J.D., G.R., J.v.d.B., and F.M. designed experiments; J.D., G.R., and J.v.d.B. performed and analyzed experiments; V.B., J.v.d.B., G.R., V.v.B., and M.A.V. performed bioinformatic analyses; J.F., I.K.M., R.M., and J.C. performed experiments; C.A. and C.S. performed live microscopy and FISH under S.L.S. supervision; C.B. and S.d.S. performed mass spectrometry under M.V.-A. supervision. R.B.T. performed fiber assays under M.A.T.M.v.V. supervision. S.G.M. shared preliminary data. I.K.M., A.B., A.G., and A.v.O. provided advice. F.M., S.L.S., and A.v.O. funded the research. F.M., J.D., G.R., and J.v.d.B. wrote the manuscript with input from all authors.

DECLARATION OF INTERESTS

A.G. is co-founder and chief scientific officer (CSO) of Ankrin Therapeutics. A.G. is a member of the scientific advisory board of *Molecular Cell*. C.B., S.d.S., and M.A.V. are employees of MOLEQLAR Analytics GmbH.

STAR★METHODS

Detailed methods are provided in the online version of this paper and include the following:

- KEY RESOURCES TABLE
- EXPERIMENTAL MODEL AND STUDY PARTICIPANT DETAILS
- METHOD DETAILS
  - ○ Genome editing
  - ○ Cell synchronization
  - ○ Drug treatments
  - ○ Gene knockdown using siRNAs
  - ○ Western blotting
  - ○ Flow cytometry
  - ○ Repli-ATAC-seq and ATAC-seq
  - ○ scEdU-seq
  - ○ scVASA-seq
  - ○ ChIC-seq
  - ○ Microscopy
  - ○ RNA FISH
  - ○ Quantitative mass spectrometry
  - ○ Analysis of senescence-associated β-galactosidase activity
  - ○ Cell-growth competition assay
  - ○ DNA fiber assay
- QUANTIFICATION AND STATISTICAL ANALYSIS

REFERENCES

1. Yadav, T., Quivy, J.-P., and Almouzni, G. (2018). Chromatin plasticity: A versatile landscape that underlies cell fate and identity. Science *361*, 1332–1336. https://doi.org/10.1126/science.aat8950.

2. Millán-Zambrano, G., Burton, A., Bannister, A.J., and Schneider, R. (2022). Histone post-translational modifications — cause and consequence of genome function. Nat. Rev. Genet. *23*, 563–580. https://doi.org/10.1038/s41576-022-00468-7.

3. Escobar, T.M., Loyola, A., and Reinberg, D. (2021). Parental nucleosome segregation and the inheritance of cellular identity. Nat. Rev. Genet. *22*, 379–392. https://doi.org/10.1038/s41576-020-00312-w.

4. Stewart-Morgan, K.R., Petryk, N., and Groth, A. (2020). Chromatin replication and epigenetic cell memory. Nat. Cell Biol. *22*, 361–371. https://doi.org/10.1038/s41556-020-0487-y.

5. Du, W., Shi, G., Shan, C.-M., Li, Z., Zhu, B., Jia, S., Li, Q., and Zhang, Z. (2022). Mechanisms of chromatin-based epigenetic inheritance. Sci. China Life Sci. *65*, 2162–2190. https://doi.org/10.1007/s11427-022-2120-1.

6. Ye, X., and Adams, P.D. (2003). Coordination of S-Phase Events and Genome Stability. Cell Cycle *2*, 185–187. https://doi.org/10.4161/cc.2.3.389.

7. MacAlpine, D.M., and Almouzni, G. (2013). Chromatin and DNA Replication. Cold Spring Harb. Perspect. Biol. *5*, a010207. https://doi.org/10.1101/cshperspect.a010207.

8. Mendiratta, S., Gatto, A., and Almouzni, G. (2019). Histone supply: Multitiered regulation ensures chromatin dynamics throughout the cell cycle. J. Cell Biol. *218*, 39–54. https://doi.org/10.1083/jcb.201807179.

9. Verreault, A., Kaufman, P.D., Kobayashi, R., and Stillman, B. (1996). Nucleosome assembly by a complex of CAF-1 and acetylated histones H3/H4. Cell *87*, 95–104. https://doi.org/10.1016/S0092-8674(00)81326-4.

10. Sobel, R.E., Cook, R.G., Perry, C.A., Annunziato, A.T., and Allis, C.D. (1995). Conservation of deposition-related acetylation sites in newly synthesized histones H3 and H4. Proc. Natl. Acad. Sci. USA *92*, 1237–1241. https://doi.org/10.1073/pnas.92.4.1237.

11. Alabert, C., and Groth, A. (2012). Chromatin replication and epigenome maintenance. Nat. Rev. Mol. Cell Biol. *13*, 153–167. https://doi.org/10.1038/nrm3288.

12. Alabert, C., Barth, T.K., Reverón-Gómez, N., Sidoli, S., Schmidt, A., Jensen, O.N., Imhof, A., and Groth, A. (2015). Two distinct modes for propagation of histone PTMs across the cell cycle. Genes Dev. *29*, 585–590. https://doi.org/10.1101/gad.256354.114.

13. Bandau, S., Alvarez, V., Jiang, H., Graff, S., Sundaramoorthy, R., Gierlinski, M., Toman, M., Owen-Hughes, T., Sidoli, S., Lamond, A., et al. (2024). RNA polymerase II promotes the organization of chromatin following DNA replication. EMBO Rep. *25*, 1387–1414. https://doi.org/10.1038/s44319-024-00085-x.

14. Alvarez, V., Bandau, S., Jiang, H., Rios-Szwed, D., Hukelmann, J., Garcia-Wilson, E., Wiechens, N., Griesser, E., Ten Have, S., Owen-Hughes, T., et al. (2023). Proteomic profiling reveals distinct phases to the restoration of chromatin following DNA replication. Cell Rep. *42*, 111996. https://doi.org/10.1016/j.celrep.2023.111996.

15. Alabert, C., Jasencakova, Z., and Groth, A. (2017). Chromatin replication and histone dynamics. Adv. Exp. Med. Biol. *1042*, 311–333. https://doi.org/10.1007/978-981-10-6955-0_15.

16. Hammond, C.M., Strømme, C.B., Huang, H., Patel, D.J., and Groth, A. (2017). Histone chaperone networks shaping chromatin function. Nat. Rev. Mol. Cell Biol. *18*, 141–158. https://doi.org/10.1038/nrm.2016.159.

17. Groth, A., Corpet, A., Cook, A.J.L., Roche, D., Bartek, J., Lukas, J., and Almouzni, G. (2007). Regulation of replication fork progression through histone supply and demand. Science *318*, 1928–1931. https://doi.org/10.1126/science.1148992.

18. Duronio, R.J., and Marzluff, W.F. (2017). Coordinating cell cycle-regulated histone gene expression through assembly and function of the Histone Locus Body. RNA Biol. *14*, 726–738. https://doi.org/10.1080/15476286.2016.1265198.

19. Saldivar, J.C., Hamperl, S., Bocek, M.J., Chung, M., Bass, T.E., Cisneros-Soberanis, F., Samejima, K., Xie, L., Paulson, J.R., Earnshaw, W.C., et al. (2018). An intrinsic S/G$_2$ checkpoint enforced by ATR. Science *361*, 806–810. https://doi.org/10.1126/science.aap9346.

20. Ye, X., Franco, A.A., Santos, H., Nelson, D.M., Kaufman, P.D., and Adams, P.D. (2003). Defective S phase chromatin assembly causes DNA damage, activation of the S phase checkpoint, and S phase arrest. Mol. Cell *11*, 341–351. https://doi.org/10.1016/S1097-2765(03)00037-6.

21. Hoek, M., and Stillman, B. (2003). Chromatin assembly factor 1 is essential and couples chromatin assembly to DNA replication in vivo. Proc. Natl. Acad. Sci. USA *100*, 12183–12188. https://doi.org/10.1073/pnas.1635158100.

22. Nabatiyan, A., and Krude, T. (2004). Silencing of chromatin assembly factor 1 in human cells leads to cell death and loss of chromatin assembly during DNA synthesis. Mol. Cell. Biol. *24*, 2853–2862. https://doi.org/10.1128/MCB.24.7.2853.

23. Günesdogan, U., Jäckle, H., and Herzig, A. (2014). Histone supply regulates S phase timing and cell cycle progression. eLife *3*, e02443. https://doi.org/10.7554/eLife.02443.

24. Franklin, R., Murn, J., and Cheloufi, S. (2021). Cell Fate Decisions in the Wake of Histone H3 Deposition. Front. Cell Dev. Biol. *9*, 654915. https://doi.org/10.3389/fcell.2021.654915.

25. Mejlvang, J., Feng, Y., Alabert, C., Neelsen, K.J., Jasencakova, Z., Zhao, X., Lees, M., Sandelin, A., Pasero, P., Lopes, M., et al. (2014). New histone supply regulates replication fork speed and PCNA unloading. J. Cell Biol. *204*, 29–43. https://doi.org/10.1083/jcb.201305017.

26. Houlard, M., Berlivet, S., Probst, A.V., Quivy, J.P., Héry, P., Almouzni, G., and Gérard, M. (2006). CAF-1 is essential for heterochromatin organization in pluripotent embryonic cells. PLoS Genet. *2*, e181. https://doi.org/10.1371/journal.pgen.0020181.

27. Smith, S., and Stillman, B. (1989). Purification and characterization of CAF-I, a human cell factor required for chromatin assembly during DNA replication in vitro. Cell *58*, 15–25. https://doi.org/10.1016/0092-8674(89)90398-X.

28. Smith, S., and Stillman, B. (1991). Stepwise assembly of chromatin during DNA replication in vitro. EMBO J. *10*, 971–980.

29. Kaufman, P.D., Kobayashi, R., Kessler, N., and Stillman, B. (1995). The p150 and p60 subunits of chromatin assembly factor I: A molecular link between newly synthesized histones and DNA replication. Cell *81*, 1105–1114. https://doi.org/10.1016/S0092-8674(05)80015-7.

30. Kamakaka, R.T., Bulger, M., Kaufman, P.D., Stillman, B., and Kadonaga, J.T. (1996). Postreplicative chromatin assembly by Drosophila and human chromatin assembly factor 1. Mol. Cell. Biol. *16*, 810–817. https://doi.org/10.1128/MCB.16.3.810.

31. Tyler, J.K., Adams, C.R., Chen, S.R., Kobayashi, R., Kamakaka, R.T., and Kadonaga, J.T. (1999). The RCAF complex mediates chromatin assembly during DNA replication and repair. Nature *402*, 555–560. https://doi.org/10.1038/990147.

32. Shibahara, K.I., and Stillman, B. (1999). Replication-dependent marking of DNA by PCNA facilitates CAF-1-coupled inheritance of chromatin. Cell *96*, 575–585. https://doi.org/10.1016/S0092-8674(00)80661-3.

33. Moggs, J.G., Grandi, P., Quivy, J.P., Jónsson, Z.O., Hübscher, U., Becker, P.B., and Almouzni, G. (2000). A CAF-1-PCNA-Mediated Chromatin Assembly Pathway Triggered by Sensing DNA Damage. Mol. Cell. Biol. *20*, 1206–1218. https://doi.org/10.1128/MCB.20.4.1206-1218.2000.

34. Rouillon, C., Eckhardt, B.V., Kollenstart, L., Gruss, F., Verkennis, A.E.E., Rondeel, I., Krijger, P.H.L., Ricci, G., Biran, A., van Laar, T., et al. (2023). CAF-1 deposits newly synthesized histones during DNA replication using distinct mechanisms on the leading and lagging strands. Nucleic Acids Res. *51*, 3770–3792. https://doi.org/10.1093/nar/gkad171.

35. Ouasti, F., Audin, M., Fréon, K., Quivy, J.-P., Tachekort, M., Cesard, E., Thureau, A., Ropars, V., Fernández Varela, P., Moal, G., et al. (2024). Disordered regions and folded modules in CAF-1 promote histone deposition in Schizosaccharomyces pombe. eLife *12*, RP91461. https://doi.org/10.7554/eLife.91461.

36. Zhang, Z., Shibahara, K.I., and Stillman, B. (2000). PCNA connects DNA replication to epigenetic inheritance in yeast. Nature *408*, 221–225. https://doi.org/10.1038/35041601.

37. Cheng, L., Zhang, X., Wang, Y., Gan, H., Xu, X., Lv, X., Hua, X., Que, J., Ordog, T., and Zhang, Z. (2019). Chromatin Assembly Factor 1 (CAF-1) facilitates the establishment of facultative heterochromatin during pluripotency exit. Nucleic Acids Res. *47*, 11114–11131. https://doi.org/10.1093/nar/gkz858.

38. Krawitz, D.C., Kama, T., and Kaufman, P.D. (2002). Chromatin assembly factor I mutants defective for PCNA binding require Asf1/Hir proteins for silencing. Mol. Cell. Biol. *22*, 614–625. https://doi.org/10.1128/MCB.22.2.614.

39. Rolef Ben-Shahar, T.R., Castillo, A.G., Osborne, M.J., Borden, K.L.B., Kornblatt, J., and Verreault, A. (2009). Two Fundamentally Distinct PCNA Interaction Peptides Contribute to Chromatin Assembly Factor 1 Function. Mol. Cell. Biol. *29*, 6353–6365. https://doi.org/10.1128/MCB.01051-09.

40. Gérard, A., Koundrioukoff, S., Ramillon, V., Sergère, J.C., Mailand, N., Quivy, J.P., and Almouzni, G. (2006). The replication kinase Cdc7-Dbf4 promotes the interaction of the p150 subunit of chromatin assembly factor 1 with proliferating cell nuclear antigen. EMBO Rep. *7*, 817–823. https://doi.org/10.1038/sj.embor.7400750.

41. Murzina, N., Verreault, A., Laue, E., and Stillman, B. (1999). Heterochromatin dynamics in mouse cells: Interaction between chromatin assembly factor 1 and HP1 proteins. Mol. Cell *4*, 529–540. https://doi.org/10.1016/S1097-2765(00)80204-X.

42. Quivy, J.-P.P., Gérard, A., Cook, A.J.L.L., Roche, D., and Almouzni, G. (2008). The HP1-p150/CAF-1 interaction is required for pericentric heterochromatin replication and S-phase progression in mouse cells. Nat. Struct. Mol. Biol. *15*, 972–979. https://doi.org/10.1038/nsmb.1470.

43. Quivy, J.P., Roche, D., Kirschner, D., Tagami, H., Nakatani, Y., and Almouzni, G. (2004). A CAF-1 dependent pool of HP1 during heterochromatin duplication. EMBO J. *23*, 3516–3526. https://doi.org/10.1038/sj.emboj.7600362.

44. Loyola, A., Tagami, H., Bonaldi, T., Roche, D., Quivy, J.P., Imhof, A., Nakatani, Y., Dent, S.Y.R., and Almouzni, G. (2009). The HP1α-CAF1-SetDB1-containing complex provides H3K9me1 for Suv39-mediated K9me3 in pericentric heterochromatin. EMBO Rep. *10*, 769–775. https://doi.org/10.1038/embor.2009.90.

45. Fischer, S., Prykhozhij, S., Rau, M.J., and Neumann, C.J. (2007). Mutation of zebrafish caf-1b results in S phase arrest, defective differentiation, and p53-mediated apoptosis during organogenesis. Cell Cycle *6*, 2962–2969. https://doi.org/10.4161/cc.6.23.4950.

46. Klapholz, B., Dietrich, B.H., Schaffner, C., Hérédia, F., Quivy, J.P., Almouzni, G., and Dostatni, N. (2009). CAF-1 is required for efficient replication of euchromatic DNA in Drosophila larval endocycling cells.

Chromosoma *118*, 235–248. https://doi.org/10.1007/s00412-008-0192-2.

47. Song, Y., He, F., Xie, G., Guo, X., Xu, Y., Chen, Y., Liang, X., Stagljar, I., Egli, D., Ma, J., et al. (2007). CAF-1 is essential for Drosophila development and involved in the maintenance of epigenetic memory. Dev. Biol. *311*, 213–222. https://doi.org/10.1016/j.ydbio.2007.08.039.

48. Franklin, R., Guo, Y., He, S., Chen, M., Ji, F., Zhou, X., Frankhouser, D., Do, B.T., Chiem, C., Jang, M., et al. (2022). Regulation of chromatin accessibility by the histone chaperone CAF-1 sustains lineage fidelity. Nat. Commun. *13*, 2350. https://doi.org/10.1038/s41467-022-29730-6.

49. Cheloufi, S., Elling, U., Hopfgartner, B., Jung, Y.L., Murn, J., Ninova, M., Hubmann, M., Badeaux, A.I., Euong Ang, C., Tenen, D., et al. (2015). The histone chaperone CAF-1 safeguards somatic cell identity. Nature *528*, 218–224. https://doi.org/10.1038/nature15749.

50. Ishiuchi, T., Enriquez-Gasca, R., Mizutani, E., Bošković, A., Ziegler-Birling, C., Rodriguez-Terrones, D., Wakayama, T., Vaquerizas, J.M., and Torres-Padilla, M.E. (2015). Early embryonic-like cells are induced by downregulating replication-dependent chromatin assembly. Nat. Struct. Mol. Biol. *22*, 662–671. https://doi.org/10.1038/nsmb.3066.

51. Ramachandran, S., and Henikoff, S. (2016). Transcriptional Regulators Compete with Nucleosomes Post-replication. Cell *165*, 580–592. https://doi.org/10.1016/j.cell.2016.02.062.

52. Nakano, S., Stillman, B., and Horvitz, H.R. (2011). Replication-coupled chromatin assembly generates a neuronal bilateral asymmetry in C. elegans. Cell *147*, 1525–1536. https://doi.org/10.1016/j.cell.2011.11.053.

53. Nabet, B., Roberts, J.M., Buckley, D.L., Paulk, J., Dastjerdi, S., Yang, A., Leggett, A.L., Erb, M.A., Lawlor, M.A., Souza, A., et al. (2018). The dTAG system for immediate and target-specific protein degradation. Nat. Chem. Biol. *14*, 431–441. https://doi.org/10.1038/s41589-018-0021-8.

54. Natsume, T., Kiyomitsu, T., Saga, Y., and Kanemaki, M.T. (2016). Rapid Protein Depletion in Human Cells by Auxin-Inducible Degron Tagging with Short Homology Donors. Cell Rep. *15*, 210–218. https://doi.org/10.1016/j.celrep.2016.03.001.

55. Liu, C.-P., Yu, Z., Xiong, J., Hu, J., Song, A., Ding, D., Yu, C., Yang, N., Wang, M., Yu, J., et al. (2023). Structural insights into histone binding and nucleosome assembly by chromatin assembly factor-1. Science *381*, eadd8673. https://doi.org/10.1126/science.add8673.

56. Mattiroli, F., Gu, Y., Yadav, T., Balsbaugh, J.L.J.L., Harris, M.R.M.R., Findlay, E.S.E.S., Liu, Y., Radebaugh, C.A.C.A., Stargell, L.A.L.A., Ahn, N.G.N.G., et al. (2017). DNA-mediated association of two histone-bound complexes of yeast chromatin assembly factor-1 (CAF-1) drives tetrasome assembly in the wake of DNA replication. eLife *6*, e22799. https://doi.org/10.7554/eLife.22799.

57. Sauer, P.V., Timm, J., Liu, D., Sitbon, D., Boeri-Erba, E., Velours, C., Mücke, N., Langowski, J., Ochsenbein, F., Almouzni, G., et al. (2017). Insights into the molecular architecture and histone H3-H4 deposition mechanism of yeast chromatin assembly factor 1. eLife *6*, 835–839. https://doi.org/10.7554/eLife.23474.

58. Liu, W.H., Roemer, S.C., Zhou, Y., Shen, Z.J., Dennehey, B.K., Balsbaugh, J.L., Liddle, J.C., Nemkov, T., Ahn, N.G., Hansen, K.C., et al. (2016). The Cac1 subunit of histone chaperone CAF-1 organizes CAF-1-H3/H4 architecture and tetramerizes histones. eLife *5*, 2852–2861. https://doi.org/10.7554/eLife.18023.001.

59. van den Berg, J., van Batenburg, V., Geisenberger, C., Tjeerdsma, R.B., de Jaime-Soguero, A., Acebrón, S.P., van Vugt, M.A.T.M., and van Oudenaarden, A. (2024). Quantifying DNA replication speeds in single cells by scEdU-seq. Nat. Methods *21*, 1175–1184. https://doi.org/10.1038/s41592-024-02308-4.

60. Rhind, N., and Gilbert, D.M. (2013). DNA Replication Timing. Cold Spring Harb. Perspect. Biol. *5*, a010132. https://doi.org/10.1101/cshperspect.a010132.

61. Spencer, S.L., Cappell, S.D., Tsai, F.C., Overton, K.W., Wang, C.L., and Meyer, T. (2013). The proliferation-quiescence decision is controlled by a

62. Trotter, E.W., and Hagan, I.M. (2020). Release from cell cycle arrest with Cdk4/6 inhibitors generates highly synchronized cell cycle progression in human cell culture. Open Biol. *10*, 200200. https://doi.org/10.1098/rsob.200200.

63. Lee, K.Y., Fu, H., Aladjem, M.I., and Myung, K. (2013). ATAD5 regulates the lifespan of DNA replication factories by modulating PCNA level on the chromatin. J. Cell Biol. *200*, 31–44. https://doi.org/10.1083/jcb.201206084.

64. Bellelli, R., Belan, O., Pye, V.E., Clement, C., Maslen, S.L., Skehel, J.M., Cherepanov, P., Almouzni, G., and Boulton, S.J. (2018). POLE3-POLE4 Is a Histone H3-H4 Chaperone that Maintains Chromatin Integrity during DNA Replication. Mol. Cell *72*, 112–126.e5. https://doi.org/10.1016/j.molcel.2018.08.043.

65. Salmen, F., De Jonghe, J., Kaminski, T.S., Alemany, A., Parada, G.E., Verity-Legg, J., Yanagida, A., Kohler, T.N., Battich, N., van den Brekel, F., et al. (2022). High-throughput total RNA sequencing in single cells using VASA-seq. Nat. Biotechnol. *40*, 1780–1793. https://doi.org/10.1038/s41587-022-01361-8.

66. Mannironi, C., Bonner, W.M., and Hatch, C.L. (1989). H2A.X. a histone isoprotein with a conserved C-terminal sequence, is encoded by a novel mRNA with both DNA replication type and polyA 3′ processing signals. Nucleic Acids Res. *17*, 9113–9126. https://doi.org/10.1093/nar/17.22.9113.

67. Mendiratta, S., Ray-Gallet, D., Lemaire, S., Gatto, A., Forest, A., Kerlin, M.A., and Almouzni, G. (2024). Regulation of replicative histone RNA metabolism by the histone chaperone ASF1. Mol. Cell *84*, 791–801.e6. https://doi.org/10.1016/j.molcel.2023.12.038.

68. Nelson, D.M., Ye, X., Hall, C., Santos, H., Ma, T., Kao, G.D., Yen, T.J., Harper, J.W., and Adams, P.D. (2002). Coupling of DNA Synthesis and Histone Synthesis in S Phase Independent of Cyclin/cdk2 Activity. Mol. Cell. Biol. *22*, 7459–7472. https://doi.org/10.1128/MCB.22.21.7459-7472.2002.

69. Armstrong, C., Passanisi, V.J., Ashraf, H.M., and Spencer, S.L. (2023). Cyclin E/CDK2 and feedback from soluble histone protein regulate the S phase burst of histone biosynthesis. Cell Rep. *42*, 112768. https://doi.org/10.1016/j.celrep.2023.112768.

70. Marzluff, W.F., and Koreski, K.P. (2017). Birth and Death of Histone mRNAs. Trends Genet. *33*, 745–759. https://doi.org/10.1016/j.tig.2017.07.014.

71. Marzluff, W.F., and Duronio, R.J. (2002). Histone mRNA expression: Multiple levels of cell cycle regulation and important developmental consequences. Curr. Opin. Cell Biol. *14*, 692–699. https://doi.org/10.1016/S0955-0674(02)00387-3.

72. Völker-Albert, M.C., Schmidt, A., Barth, T.K., Forne, I., and Imhof, A. (2018). Detection of Histone Modification Dynamics during the Cell Cycle by MS-Based Proteomics. In Histone Variants (Humana Press), pp. 61–74. https://doi.org/10.1007/978-1-4939-8663-7_4.

73. Loyola, A., Bonaldi, T., Roche, D., Imhof, A., and Almouzni, G. (2006). PTMs on H3 Variants before Chromatin Assembly Potentiate Their Final Epigenetic State. Mol. Cell *24*, 309–316. https://doi.org/10.1016/j.molcel.2006.08.019.

74. Ray-Gallet, D., Woolfe, A., Vassias, I., Pellentz, C., Lacoste, N., Puri, A., Schultz, D.C., Pchelintsev, N.A., Adams, P.D., Jansen, L.E.T., et al. (2011). Dynamics of Histone H3 Deposition In Vivo Reveal a Nucleosome Gap-Filling Mechanism for H3.3 to Maintain Chromatin Integrity. Mol. Cell *44*, 928–941. https://doi.org/10.1016/j.molcel.2011.12.006.

75. Ishiuchi, T., Abe, S., Inoue, K., Yeung, W.K.A., Miki, Y., Ogura, A., and Sasaki, H. (2021). Reprogramming of the histone H3.3 landscape in the early mouse embryo. Nat. Struct. Mol. Biol. *28*, 38–49. https://doi.org/10.1038/s41594-020-00521-1.

76. Alabert, C., Loos, C., Voelker-Albert, M., Graziano, S., Forné, I., Reveron-Gomez, N., Schuh, L., Hasenauer, J., Marr, C., Imhof, A., et al. (2020). Domain Model Explains Propagation Dynamics and Stability of Histone H3K27 and H3K36 Methylation Landscapes. Cell Rep. *30*, 1223–1234.e8. https://doi.org/10.1016/j.celrep.2019.12.060.

77. Saredi, G., Huang, H., Hammond, C.M., Alabert, C., Bekker-Jensen, S., Forne, I., Reverón-Gómez, N., Foster, B.M., Mlejnkova, L., Bartke, T., et al. (2016). H4K20me0 marks post-replicative chromatin and recruits the TONSL-MMS22L DNA repair complex. Nature *534*, 714–718. https://doi.org/10.1038/nature18312.

78. Pellegrino, S., Michelena, J., Teloni, F., Imhof, R., and Altmeyer, M. (2017). Replication-Coupled Dilution of H4K20me2 Guides 53BP1 to Pre-replicative Chromatin. Cell Rep. *19*, 1819–1831. https://doi.org/10.1016/j.celrep.2017.05.016.

79. Simonetta, M., de Krijger, I., Serrat, J., Moatti, N., Fortunato, D., Hoekman, L., Bleijerveld, O.B., Altelaar, A.F.M., and Jacobs, J.J.L. (2018). H4K20me2 distinguishes pre-replicative from post-replicative chromatin to appropriately direct DNA repair pathway choice by 53BP1-RIF1-MAD2L2. Cell Cycle *17*, 124–136. https://doi.org/10.1080/15384101.2017.1404210.

80. Scharf, A.N.D., Meier, K., Seitz, V., Kremmer, E., Brehm, A., and Imhof, A. (2009). Monomethylation of Lysine 20 on Histone H4 Facilitates Chromatin Maturation. Mol. Cell. Biol. *29*, 57–67. https://doi.org/10.1128/MCB.00989-08.

81. Stewart-Morgan, K.R., Reverón-Gómez, N., and Groth, A. (2019). Transcription Restart Establishes Chromatin Accessibility after DNA Replication. Mol. Cell *75*, 284–297.e6. https://doi.org/10.1016/j.molcel.2019.04.033.

82. Chen, B., MacAlpine, H.K., Hartemink, A.J., and MacAlpine, D.M. (2023). Spatiotemporal kinetics of CAF-1-dependent chromatin maturation ensures transcription fidelity during S-phase. Genome Res. *33*, 2108–2118. https://doi.org/10.1101/gr.278273.123.

83. Topal, S., Vasseur, P., Radman-Livaja, M., and Peterson, C.L. (2019). Distinct transcriptional roles for Histone H3-K56 acetylation during the cell cycle in Yeast. Nat. Commun. *10*, 4372. https://doi.org/10.1038/s41467-019-12400-5.

84. Jiang, D., and Berger, F. (2017). DNA replication–coupled histone modification maintains Polycomb gene silencing in plants. Science *357*, 1146–1149. https://doi.org/10.1126/science.aan4965.

85. Zeller, P., Yeung, J., Viñas Gaza, H., de Barbanson, B.A., Bhardwaj, V., Florescu, M., van der Linden, R., and van Oudenaarden, A. (2023). Single-cell sortChIC identifies hierarchical chromatin dynamics during hematopoiesis. Nat. Genet. *55*, 333–345. https://doi.org/10.1038/s41588-022-01260-3.

86. Riba, A., Oravecz, A., Durik, M., Jiménez, S., Alunni, V., Cerciat, M., Jung, M., Keime, C., Keyes, W.M., and Molina, N. (2022). Cell cycle gene regulation dynamics revealed by RNA velocity and deep-learning. Nat. Commun. *13*, 2865. https://doi.org/10.1038/s41467-022-30545-8.

87. Sokolova, M., Turunen, M., Mortusewicz, O., Kivioja, T., Herr, P., Vähärautio, A., Björklund, M., Taipale, M., Helleday, T., and Taipale, J. (2017). Genome-wide screen of cell-cycle regulators in normal and tumor cells identifies a differential response to nucleosome depletion. Cell Cycle *16*, 189–199. https://doi.org/10.1080/15384101.2016.1261765.

88. Kang, M.-S., Kim, J., Ryu, E., Ha, N.Y., Hwang, S., Kim, B.-G., Ra, J.S., Kim, Y.J., Hwang, J.M., Myung, K., et al. (2019). PCNA Unloading Is Negatively Regulated by BET Proteins. Cell Rep. *29*, 4632–4645.e5. https://doi.org/10.1016/j.celrep.2019.11.114.

89. McPherson, J.E., Grossmann, L.C., Salzler, H.R., Armstrong, R.L., Kwon, E., Matera, A.G., McKay, D.J., and Duronio, R.J. (2023). Reduced histone gene copy number disrupts Drosophila Polycomb function. Genetics *224*, iyad106. https://doi.org/10.1093/genetics/iyad106.

90. Blackledge, N.P., and Klose, R.J. (2021). The molecular principles of gene regulation by Polycomb repressive complexes. Nat. Rev. Mol. Cell Biol. *22*, 815–833. https://doi.org/10.1038/s41580-021-00398-y.

91. Yu, J.-R., Lee, C.-H., Oksuz, O., Stafford, J.M., and Reinberg, D. (2019). PRC2 is high maintenance. Genes Dev. *33*, 903–935. https://doi.org/10.1101/gad.325050.119.

92. Chen, P., Zhao, J., Wang, Y., Wang, M., Long, H., Liang, D., Huang, L., Wen, Z., Li, W., Li, X., et al. (2013). H3.3 actively marks enhancers and primes gene transcription via opening higher-ordered chromatin. Genes Dev. *27*, 2109–2124. https://doi.org/10.1101/gad.222174.113.

93. Liu, C., Yu, J., Song, A., Wang, M., Hu, J., Chen, P., Zhao, J., and Li, G. (2023). Histone H1 facilitates restoration of H3K27me3 during DNA replication by chromatin compaction. Nat. Commun. *14*, 4081. https://doi.org/10.1038/s41467-023-39846-y.

94. Carraro, M., Hendriks, I.A., Hammond, C.M., Solis-Mezarino, V., Völker-Albert, M., Elsborg, J.D., Weisser, M.B., Spanos, C., Montoya, G., Rappsilber, J., et al. (2023). DAXX adds a de novo H3.3K9me3 deposition pathway to the histone chaperone network. Mol. Cell *83*, 1075–1092.e9. https://doi.org/10.1016/j.molcel.2023.02.009.

95. Navarro, C., Lyu, J., Katsori, A.-M., Caridha, R., and Elsässer, S.J. (2020). An embryonic stem cell-specific heterochromatin state promotes core histone exchange in the absence of DNA accessibility. Nat. Commun. *11*, 5095. https://doi.org/10.1038/s41467-020-18863-1.

96. Ostrowski, M.S., Yang, M.G., McNally, C.P., Abdulhay, N.J., Wang, S., Nora, E.P., Goodarzi, H., and Ramani, V. (2023). The single-molecule accessibility landscape of newly replicated mammalian chromatin. Preprint at bioRxiv. https://doi.org/10.1101/2023.10.09.561582.

97. Reverón-Gómez, N., González-Aguilera, C., Stewart-Morgan, K.R., Petryk, N., Flury, V., Graziano, S., Johansen, J.V., Jakobsen, J.S., Alabert, C., and Groth, A. (2018). Accurate Recycling of Parental Histones Reproduces the Histone Modification Landscape during DNA Replication. Mol. Cell *72*, 239–249.e5. https://doi.org/10.1016/j.molcel.2018.08.010.

98. Liu, Y., Zhangding, Z., Liu, X., Gan, T., Ai, C., Wu, J., Liang, H., Chen, M., Guo, Y., Lu, R., et al. (2024). Fork coupling directs DNA replication elongation and termination. Science *383*, 1215–1222. https://doi.org/10.1126/science.adj7606.

99. Gaggioli, V., Lo, C.S.Y., Reverón-Gómez, N., Jasencakova, Z., Domenech, H., Nguyen, H., Sidoli, S., Tvardovskiy, A., Uruci, S., Slotman, J.A., et al. (2023). Dynamic de novo heterochromatin assembly and disassembly at replication forks ensures fork stability. Nat. Cell Biol. *25*, 1017–1032. https://doi.org/10.1038/s41556-023-01167-z.

100. Replogle, J.M., Saunders, R.A., Pogson, A.N., Hussmann, J.A., Lenail, A., Guna, A., Mascibroda, L., Wagner, E.J., Adelman, K., Lithwick-Yanai, G., et al. (2022). Mapping information-rich genotype-phenotype landscapes with genome-scale Perturb-seq. Cell *185*, 2559–2575.e28. https://doi.org/10.1016/j.cell.2022.05.013.

101. Ng, C., Aichinger, M., Nguyen, T., Au, C., Najar, T., Wu, L., Mesa, K.R., Liao, W., Quivy, J.-P., Hubert, B., et al. (2019). The histone chaperone CAF-1 cooperates with the DNA methyltransferases to maintain *Cd4* silencing in cytotoxic T cells. Genes Dev. *33*, 669–683. https://doi.org/10.1101/gad.322024.118.

102. Flavahan, W.A., Gaskell, E., and Bernstein, B.E. (2017). Epigenetic plasticity and the hallmarks of cancer. Science *357*, eaal2380. https://doi.org/10.1126/science.aal2380.

103. Buenrostro, J.D., Giresi, P.G., Zaba, L.C., Chang, H.Y., and Greenleaf, W.J. (2013). Transposition of native chromatin for fast and sensitive epigenomic profiling of open chromatin, DNA-binding proteins and nucleosome position. Nat. Methods *10*, 1213–1218. https://doi.org/10.1038/nmeth.2688.

104. Dull, T., Zufferey, R., Kelly, M., Mandel, R.J., Nguyen, M., Trono, D., and Naldini, L. (1998). A Third-Generation Lentivirus Vector with a Conditional Packaging System. J. Virol. *72*, 8463–8471. https://doi.org/10.1128/JVI.72.11.8463-8471.1998.

105. Stewart, S.A., Dykxhoorn, D.M., Palliser, D., Mizuno, H., Yu, E.Y., An, D.S., Sabatini, D.M., Chen, I.S.Y., Hahn, W.C., Sharp, P.A., et al.

(2003). Lentivirus-delivered stable gene silencing by RNAi in primary cells. RNA *9*, 493–501. https://doi.org/10.1261/rna.2192803.

106. Bhardwaj, V., Heyne, S., Sikora, K., Rabbani, L., Rauer, M., Kilpert, F., Richter, A.S., Ryan, D.P., and Manke, T. (2019). snakePipes: facilitating flexible, scalable and integrative epigenomic analysis. Bioinformatics *35*, 4757–4759. https://doi.org/10.1093/bioinformatics/btz436.

107. Ramírez, F., Ryan, D.P., Grüning, B., Bhardwaj, V., Kilpert, F., Richter, A.S., Heyne, S., Dündar, F., and Manke, T. (2016). deepTools2: a next generation web server for deep-sequencing data analysis. Nucleic Acids Res. *44*, W160–W165. https://doi.org/10.1093/nar/gkw257.

108. Langmead, B., and Salzberg, S.L. (2012). Fast gapped-read alignment with Bowtie 2. Nat. Methods *9*, 357–359. https://doi.org/10.1038/nmeth.1923.

109. Li, H., Handsaker, B., Wysoker, A., Fennell, T., Ruan, J., Homer, N., Marth, G., Abecasis, G., and Durbin, R.; 1000 Genome Project Data Processing Subgroup (2009). The Sequence Alignment/Map format and SAMtools. Bioinformatics *25*, 2078–2079. https://doi.org/10.1093/bioinformatics/btp352.

110. Tarasov, A., Vilella, A.J., Cuppen, E., Nijman, I.J., and Prins, P. (2015). Sambamba: fast processing of NGS alignment formats. Bioinformatics *31*, 2032–2034. https://doi.org/10.1093/bioinformatics/btv098.

111. Stuart, T., Butler, A., Hoffman, P., Hafemeister, C., Papalexi, E., Mauck, W.M., Hao, Y., Stoeckius, M., Smibert, P., and Satija, R. (2019). Comprehensive Integration of Single-Cell Data. Cell *177*, 1888–1902.e21. https://doi.org/10.1016/j.cell.2019.05.031.

112. Schindelin, J., Arganda-Carreras, I., Frise, E., Kaynig, V., Longair, M., Pietzsch, T., Preibisch, S., Rueden, C., Saalfeld, S., Schmid, B., et al. (2012). Fiji: an open-source platform for biological-image analysis. Nat. Methods *9*, 676–682. https://doi.org/10.1038/nmeth.2019.

113. MacLean, B., Tomazela, D.M., Shulman, N., Chambers, M., Finney, G.L., Frewen, B., Kern, R., Tabb, D.L., Liebler, D.C., and MacCoss, M.J. (2010). Skyline: an open source document editor for creating and analyzing targeted proteomics experiments. Bioinformatics *26*, 966–968. https://doi.org/10.1093/bioinformatics/btq054.

114. Stewart-Morgan, K.R., and Groth, A. (2023). Profiling Chromatin Accessibility on Replicated DNA with repli-ATAC-Seq. In Chromatin Accessibility (Humana Press), pp. 71–84. https://doi.org/10.1007/978-1-0716-2899-7_6.

115. Dekker, J., Belmont, A.S., Guttman, M., Leshyk, V.O., Lis, J.T., Lomvardas, S., Mirny, L.A., O'Shea, C.C., Park, P.J., Ren, B., et al. (2017). The 4D nucleome project. Nature *549*, 219–226. https://doi.org/10.1038/nature23884.

116. Macheret, M., and Halazonetis, T.D. (2018). Intragenic origins due to short G1 phases underlie oncogene-induced DNA replication stress. Nature *555*, 112–116. https://doi.org/10.1038/nature25507.

117. Hughes, C.S., Moggridge, S., Müller, T., Sorensen, P.H., Morin, G.B., and Krijgsveld, J. (2019). Single-pot, solid-phase-enhanced sample preparation for proteomics experiments. Nat. Protoc. *14*, 68–85. https://doi.org/10.1038/s41596-018-0082-x.

Molecular Cell
Article

STAR★METHODS

KEY RESOURCES TABLE

REAGENT or RESOURCE	SOURCE	IDENTIFIER
Antibodies		
H3K9Me3	Abcam	Cat# ab8898; RRID:AB_306848
H3K27Me3	Cell Signaling Technology	Cat# 9733, C36B11; RRID:AB_2616029
CHAF1A	Cell Signaling Technology	Cat# D77D5; RRID:AB_10697028
CHAF1B	Novus Biological	Cat# NBP1-88235; RRID:AB_11017504
PCNA	Abcam	Cat# ab29; RRID:AB_303394
ATAD5	Lee et al.[63]	N/A
p53	Santa Cruz Biotechnology	Cat# sc-126; RRID:AB_628082
p21	Cell Signaling Technology	Cat# 2947; RRID:AB_823586
pCHK1 (S345)	Cell Signaling Technology	Cat# 2348; RRID:AB_331212
pCHK1 (S317)	Cell Signaling Technology	Cat# 2344; RRID:AB_331488
CHK1	Cell Signaling Technology	Cat# 2360; RRID:AB_2080320
pCHK2 (T68)	Cell Signaling Technology	Cat# 2661; RRID:AB_331479
CHK2	Cell Signaling Technology	Cat# 3440; RRID:AB_2229490
pCDK1 (T15)	Cell Signaling Technology	Cat# 9111; RRID:AB_331460
CDK1	Abcam	Cat# ab18; RRID:AB_2074906
yH2A.X (S139)	Sigma Aldrich	Cat# 05-636; RRID:AB_309864
H2A.X	Sigma Aldrich	Cat# 07-627; RRID:AB_2233033
pRPA2 (S4/8)	Fortis Life Sciences	Cat# A300-245A; RRID:AB_210547
RPA2	Abcam	Cat# ab2175; RRID:AB_302873
Monoclonal mouse anti-BrdU	BD Biosciences	Cat# 347580; RRID:AB_10015219
Monoclonal rat anti-BrdU	Abcam	Cat# ab6326; RRID:AB_305426
Goat anti-Rat IgG, Alexa Fluor 488 conjugated	ThermoFisher	Cat# A-11006; RRID:AB_2534074
Goat anti-Mouse IgG, Alexa Fluor 647 conjugated	ThermoFisher	Cat# A32728; RRID:AB_2633277
Chemicals, peptides, and recombinant proteins		
DMEM/F-12, GlutaMAX™ supplement	Gibco	Cat# 10565018
Fetal Bovine Serum	Sigma Aldrich	Cat# 12103C
Penicillin-Streptomycin (10,000 U/mL)	Gibco	Cat# 15140122
TrypLE Express	Gibco	Cat# 12605010
Blasticidin	Invivogen	Cat# ant-bl-1
DirectPCR Lysis Reagent	Viagen Biotech	Cat# 101-T
GoTaq® G2 Flexi DNA Polymerase	Promega	Cat# M7801
Proteinase K	New England Biolabs	Cat# P8107S
Thermolabile Proteinase K	New England Biolabs	Cat# P8111S
Polybrene	Sigma Aldrich	Cat# TR-1003-G
Palbociclib	Selleck Chemicals	Cat# S1116
dTAGV-1	Tocris	Cat# 6914
IGEPAL CA-630	Sigma Aldrich	Cat# I3021
Complete™ EDTA-free Protease Inhibitor Cocktail	Roche	Cat# 5056489001
PhosSTOP	Roche	Cat# 4906845001
Benzonase® Nuclease	Millipore	Cat# 70746
4-12% Bolt™ Bis-Tris Plus Mini Protein Gels	Invitrogen	Cat# NW04127BOX
Nitrocellulose Membrane	BioRad	Cat# 1620112
Bovine Serum Albumin (BSA)	Sigma Aldrich	Cat# A7906

(Continued on next page)

Continued

REAGENT or RESOURCE	SOURCE	IDENTIFIER
SuperSignal™ West Pico PLUS Chemiluminescent Substrat	Thermo Scientific	Cat# 15659364
EdU	Abcam	Cat# ab146186
Thymidine	Sigma Aldrich	Cat# T9250-1G
Triton™ X-100	Sigma Aldrich	Cat# X100-500ML
CuSO4*5H2O	Sigma Aldrich	Cat# 209198
L-Ascorbic acid	Sigma Aldrich	Cat# A0278
AF647-Azide	Jena BioScience	Cat# CLK-1299-1
THPTA	Jena BioScience	Cat# CLK-1010-25
Picolyl-azide-PEG4-biotin	Jena BioScience	Cat# CLK-1167-5
Agencourt AMPure XP beads	Beckman Coulter	Cat# A63880
Dynabeads™ MyOne™ Streptavidin T1	Invitrogen	Cat# 10531265
NEBNext® High-Fidelity 2X PCR Master Mix	New England Biolabs	Cat# M0541S
Spermidine solution	Sigma Aldrich	Cat# S2626
Tween® 20	Sigma Aldrich	Cat# P1379
Biotin-PEG3-Azide	Sigma Aldrich	Cat# 762024
DAPI	Sigma Aldrich	Cat# D9542
NlaIII	New England Biolabs	Cat# R0125L
Dynabeads™ MyOne™ Streptavidin C1	Invitrogen	Cat# 65001
DNA Polymerase I, Large (Klenow) Fragment	New England Biolabs	Cat# M0210S
T4 Polynucleotide Kinase	New England Biolabs	Cat# M0201S
dNTPs	Promega	Cat# U1515
dATP	Promega	Cat# U1201
ATP	Thermo Scientific	Cat# R0441
PEG8000	Sigma Aldrich	Cat# 89510
T4 Polynucleotide Kinase Reaction Buffer	New England Biolabs	Cat# B0201S
AmpliTaq™ 360 DNA Polymerase	Applied Biosystems	Cat# 4398818
T4 DNA Ligase (400.000U)	New England Biolabs	Cat# M0202S
MEGAscript™ T7 Transcription Kit	Invitrogen	Cat# AM1334
TurboDNAse	Invitrogen	Cat# AM2238
RNA Clean XP beads	Beckman Coulter	Cat# A63987
RNaseOUT™ Recombinant Ribonuclease Inhibitor	Invitrogen	Cat# 10777019
SuperScript™ II Reverse Transcriptase	Invitrogen	Cat# 18064014
SuperScript™ III Reverse Transcriptase	Invitrogen	Cat# 18080044
SuperScript™ III Reverse Transcriptase	Invitrogen	Cat# 18080093
RNAseA	Thermo Scientific	Cat# R1253
NEBNext® Ultra™ II Q5® Master Mix	New England Biolabs	Cat# M0544S
EGTA	Thermo Scientific Chemicals	Cat# J60767.AE
pA-MNase	Zeller et al.[85]	N/A
E.coli Poly(A) Polymerase	New England Biolabs	Cat# M0276S
Second Strand Buffer	Invitrogen	Cat# 10812014
E.coli DNA Polymerase I	Invitrogen	Cat# 18010017
Exonuclease I	New England Biolabs	Cat# M0293S
MegaScript T7 Transcription Kit	Invitrogen	Cat# AM1333
ExoSAP-IT	Applied Biosystems	Cat# 78200.200.UL
Hybridase thermostable Rnase H	Epicentre	Cat# H39500
RQ1 RNase-Free DNase	Promega	Cat# M6101
T4 RNA Ligase 2, truncated	New England Biolabs	Cat# M0242S

Molecular Cell
Article

Continued

REAGENT or RESOURCE	SOURCE	IDENTIFIER
Kapa HiFi HotStart PCR mix	Roche	Cat# 7958927001
PureCol® Solution	Advanced BioMatrix	Cat# 5005
Hoechst 34580	Invitrogen	Cat# H21486
Fugene-HD	Promega	Cat# E2311
Histone H4.2 mRNA probe	Thermo Fisher	Cat# VA63174283VC
Aurora Elite TS 15 cm x 75 μm ID, 1.7 μm	IonOpticks	N/A
Vanquish™ Neo UHPLC System	Thermo Scientific	Cat# VN-S10-A-01
DMEM for SILAC	Thermo Scientific	Cat# A33822
L-Arginine·HCl ($^{13}C_6$, 99%)	Cambridge Isotope Laboratories, Inc	Cat# CLM-2265H-PK
L-Arginine	Sigma Aldrich	Cat# A8094
L-Lysine monohydrochloride	Sigma Aldrich	Cat# L8662
PBS pH 7.4	Gibco	Cat# 10010-015
N-(Propionyloxy)succinimide	Sigma-Aldrich	Cat# 93535-1G
cOmplete Mini EDTA-free	Roche	Cat# 1183617007
Water ROTISOLV® Ultra LC-MS	Roth	Cat# HN43.2
Ammonia solution, 25 %, Ph. Eur.	Roth	Cat# 2610.1
Acetonitrile ROTISOLV® HPLC Gradient	Roth	Cat# HN44.2
Sulfuric acid	Sigma-Aldrich	Cat# 258105
Ethanol ROTISOLV® HPLC Gradient Grade	Roth	Cat# P076.2
Triethylammonium bicarbonate buffer	Sigma-Aldrich	Cat# 90360
Ammonium hydrogen carbonate	Roth	Cat# T871.1
SPEEDBEAD MAG CARBOXYL MODIF PART, 15 ML	Sigma-Aldrich	Cat# GE45152105050250
SPEEDBEAD MAG CARBOXYL MODIF PART, 15 ML	Sigma-Aldrich	Cat# GE65152105050250
Seq Grade Modified Trypsin, lOOug (5 x 20ug)	Promega	Cat# V5111
MagneSphere® Technology Magnetic Separation Stands	Promega	Cat# Z5332
TFA, LC-MS Grade	Thermo Scientific	Cat# 85183
Spiketides (H3, H3.1 and H3.3)	JPT	N/A
Water ROTISOLV® Ultra LC-MS	Roth	Cat# HN43.2
Ammonia solution, 25 %, Ph. Eur.	Roth	Cat# 2610.1
2-Propanol ROTISOLV® ≥99,95 %, LC-MS Grade	Roth	Cat# AE73.1
Formic acid ROTIPURAN® ≥99 %, LC-MS Grade	Roth	Cat# 1EHK.3
Aurora Elite TS, 15 cm x 75 μm ID, 1.7 μm	IonOpticks	N/A
2-Propanol ROTISOLV® ≥99,95 %, LC-MS Grade	Roth	Cat# AE73.1
ATRi (AZD6738/Ceralasertib)	Selleckchem	Cat#S7693
ATMi (KU-55933)	Selleckchem	Cat#S1092
CHK1i (CHIR-124)	Selleckchem	Cat#S2683
WEE1i (MK-1775/Adavosertib)	Selleckchem	Cat#S1525
Aphidicolin	Sigma	Cat#A0781-5MG
Critical commercial assays		
Illumina Tagment DNA TDE1 Enzyme and Buffer Kits	Illumina	Cat# 20034197
Click-iT™ EdU Cell Proliferation Kit for Imaging, Alexa Fluor™ 647 dye	Invitrogen	Cat# C10340
MinElute PCR Purification Kit	Qiagen	Cat# 28006
MinElute Reaction Cleanup Kit	Qiagen	Cat# 28204
Qubit dsDNA HS Assay Kit	Invitrogen	Cat# Q33230
Agilent High Sensitivity DNA Kit + chips	Agilent	Cat# 5067-4626

Continued

REAGENT or RESOURCE	SOURCE	IDENTIFIER
Agilent RNA 6000 Pico Kit	Agilent	Cat# 5067-1513
ViewRNA ISH Cell Assay Kit	Invitrogen	Cat# QVC0001
CellEvent™ Senescence Green Flow Cytometry Assay Kit	Invitrogen	Cat# C10840
Deposited data		
Raw and analyzed sequencing data	This manuscript	GEO: GSE262518
Proteomics data	This manuscript	PRIDE: PXD050618
Raw imaging data (microscopy and western blots)	This manuscript	https://doi.org/10.17632/n9h2mj7dbg.1
Custom scripts for data analysis	This manuscript	https://doi.org/10.5281/zenodo.13918157
Experimental models: Cell lines		
TERT-RPE-1	ATCC	Cat# CRL-4000
HEK293T	ATCC	Cat# CRL-3216
S2 D.melanogaster	ATCC	Cat# CRL-1963
RPE-hTERT (dTAG-CAF1) (DHB-mVenus, H2B-mTurq2)	This manuscript	N/A
RPE-hTERT (dTAG-CAF1) (p53-KO) (DHB-mVenus, H2B-mTurq2)	This manuscript	N/A
Oligonucleotides		
RA3 /5rApp/TGGAATTCTCGGGTGCCAAGG/3SpC3/	Integrated DNA Technology	N/A
RTP GCCTTGGCACCCGAGAATTCCA	Integrated DNA Technology	N/A
CS2 random Hexamer GCCTTGGCACC CGAGAATTCCANNNNNN	Integrated DNA Technology	N/A
EdU-fill in primer ATGCCGGTAATACGACTCAC	Integrated DNA Technology	N/A
ATAC-seq oligos	Buenrostro et al.[103]	N/A
H4.2 FISH probe	ThermoFisher	VA6-3174283-VC
siCTRL 5'-UGGUUUACAUGUCGACUAA-3	This manuscript	N/A
siCDKN1A SMARTPool	Dharmacon	Cat#L-003471-00-0005
Recombinant DNA		
pUC57 FKBP12^F36V	GenScript/This manuscript	N/A
pUC57 V5 - FKBP12^F36V	GenScript/This manuscript	N/A
p225a-CHAF1A-Cas9-RNA	This manuscript	N/A
CSII-EF DHB-mVenus	Spencer et al.[61]	Addgene #136461
CSII-EF H2B-mTurquoise	Spencer et al.[61]	N/A
pMDLg	Dull et al.[104]	Addgene Cat# 12251
pRSV-Rev	Dull et al.[104]	Addgene Cat# 12253
pCMV-VSV-G	Stewart et al.[105]	Addgene Cat# 8454
Software and algorithms		
snakePipes	Bhardwaj et al.[106]	PMID: 31134269
DeepTools (v3.1)	Ramírez et al.[107]	https://deeptools.readthedocs.io/en/develop
Trim-galore (v0.6.5)	Babraham Bioinformatics	https://www.bioinformatics.babraham.ac.uk/projects/trim_galore/
Bowtie2 (v2.3)	Langmead and Salzberg[108]	https://bowtie-bio.sourceforge.net/bowtie2/index.shtml
samtools (v1.10)	Li et al.[109]	http://www.htslib.org/
sambamba (v0.7.1)	Tarasov et al.[110]	PMID: 25697820
Seurat (v5.0.1)	Stuart et al.[111]	https://satijalab.org/seurat/
R	R Project	https://www.r-project.org/
MATLAB (R2020a)	MathWorks	https://www.mathworks.com/products/matlab.html
FIJI	Schindelin et al.[112]	https://imagej.net/software/fiji

Continued

REAGENT or RESOURCE	SOURCE	IDENTIFIER
GraphPad Prism	GraphPad	https://www.graphpad.com/features
Zeiss ZEN Pro (version 3.6)	Zeiss	http://www.zeiss.com/
Skyline	MacLean et al.[113]	v22.2.0.351
Other		
Electroporation Cuvettes Plus	BTX Harvard Apparatus	Cat# BTX620
Amaxa Nucleofector II	Lonza	N/A
384-well hardshell plate	BioRad	Cat # HSP3801
Silverseal sealer	Greiner	Cat # 676090
Eppendorf® DNA LoBind Tubes, 1.5 mL	Eppendorf	Cat # 0030108051
Protein LoBind® Tubes, 1.5 mL	Eppendorf	Cat # 0030108116
Protein LoBind® Tubes, 2 mL	Eppendorf	Cat # 0030108132
twin tec PCR Plate 96, unskirted, clear (250µl)	Eppendorf	Cat # 0030 133.366
AttractSPE® Tips C8	Affinisep	Cat # C8.T2.200.96
SureStart vials amber tpx screw 9MM	Thermo Scientific	Cat#60180-1655
UIP400MTP	Hielscher Ultrasonics GmbH	N/A
Eppendorf ThermoMixer C	VWR	Cat# 5382000015
Orbitrap Exploris 240	Thermo Fisher Scientific	Cat# BRE725535
Centrifuge 5427 r	VWR	Cat# 5409000210
Eppendorf Concentrator plus	VWR	Cat# 5305000509
Vanquish Neo System	Thermo Fisher Scientific	Cat#VN-S10-A-01
Zeiss Axio Imager Z2	Zeiss	N/A

EXPERIMENTAL MODEL AND STUDY PARTICIPANT DETAILS

Human TERT-RPE-1 cells (female) were cultured in Dulbecco's Modified Eagle's Medium/Nutrient Mixture F-12, GlutaMAX™ supplement (DMEM, Gibco) containing 10% Fetal Bovine Serum (FBS, Sigma Aldrich) and 100 U/mL penicillin/streptomycin (Gibco) at 37°C in 5% CO2. Cells were passaged twice a week using TrypLE Express (Gibco) and tested regularly for the absence of mycoplasma.

METHOD DETAILS

Genome editing

FKBP12^{F36V}-CHAF1A expressing cells were generated by nucleofection of WT hTERT-RPE-1 cells with a CRISPR knockin donor vector as well as a Cas9 guideRNA vector. 3x10^5 cells were resuspended in 100 µL ice cold nucleofection buffer (20 mM HEPES pH 7.5, 5 mM KCl, 10 mM MgCl2, 90 mM Na2HPO4) and 5 µg of both CRISPR-Cas9 vectors. Nucleofection was performed using Electroporation Cuvettes Plus (BTX) and the Amaxa Nucleofector II (Lonza). One nucleofection with only the Cas9 guideRNA vector served as a negative control. Cells were seeded into DMEM and left to recover for 48hr. Then, cells were selected for two weeks with 8 µg/mL blasticidin (Invivogen) before sorted as single cells into 96-well plates (BD FACSAria Fusion). For genotyping, cells of individual clones were washed with PBS0 twice before being lysed with 2-fold diluted DirectPCR Lysis Reagent (Viagen Biotech) supplemented with 20 µg/uL Proteinase K (NEB). The lysates were incubated for 16hr at 55°C followed by 1.5hr at 85°C. The resulting gDNA was genotyped using GoTaq G2 Flexi DNA Polymerase kit (Promega) and indicated primers.

For this manuscript, we used two different clonal cell lines (clone 6 and clone 8) expressing two slightly different versions of the degron-tag (Figure S1A).

Cells stably expressing fluorescent proteins for live-microscopy experiments were generated by lentiviral transduction. For virus generation, HEK293T cells were transfected with CSII-EF DHB-mVenus and CSII-EF H2B-mTurquoise along with the packaging and envelope plasmids (pMDLg, pRSV-Rev, pCMV-VSV-G)[104,105] using Fugene-HD (Promega). Lentivirus was harvested 48hr after transfection, filtered through a 0.45 µm filter (Millipore), and incubated with target cells for 10hr with 5 µg/mL polybrene (Sigma Aldrich). Cells with stable integration were sorted on an Aria Fusion Flow Cytometer to establish a population expressing the fluorescent proteins.

Cell synchronization

To induce a G1 phase arrest, cells were cultured in DMEM medium containing 2.5% FBS and 150 nM palbociclib (Selleck Chemicals) for 24hr. For the synchronous release into S-phase, cells were washed twice with PBS0 before cultured in DMEM containing 15% FBS. To induce G2/M phase arrest, cells were treated with 300 nM nocodazole (Sigma-Aldrich) for 16 hours.

Drug treatments

Cells were treated with 500 nM or 1 μM dTAG^{V}-1 (dTAG) (Tocris) for indicated periods to induce degradation of FKBP12^{F36V}-CHAF1A fusion protein. For studies on EdU intensities in Figure 2G, cells were pre-treated with either ATRi (5 μM), ATMi (10 μM), CHK1i (1 μM) or Wee1i (0.5 μM) (all Selleck Chemicals) for 2 hr, before DMSO/dTAG was added for 1.5 hr. Finally, EdU (10 μM) was added for 30 min before cell harvest.

Gene knockdown using siRNAs

Degron-CHAF1A cells were transfected using Lipofectamine™ RNAiMAX transfection reagent (Invitrogen). For approximately 3x10⁷ cells, 2 mL of OptiMEM (Invitrogen) medium was preincubated with 10 uL of Lipofectamine™ RNAiMAX for 5 min. Next, siRNA (5 nM final concentration) was added and again incubated for 10 min before adding to the cells. 24 hr after transfection, the medium was refreshed to remove siRNAs.

Western blotting

Whole-cell extracts

Cells were harvested using TrypLE, washed once with PBS0 and pellets were lysed in RIPA buffer (25 mM Tris, 150 mM NaCl, 1% IGEPAL CA-630, 1% NaDOC, 0.1% SDS, 1x protease inhibitor and 0.5 mM DTT). The lysates were incubated on ice for 20 minutes before centrifuged at 17,000 x g for 15 minutes at 4°C. Supernatant was taken as sample for whole cell extracts. Note, when blotting for phospho-proteins, RIPA was further supplemented with 1x PhosSTOP (Roche).

Separation of soluble and chromatin fractions

Cells were harvested using TrypLE, washed once with PBS0 and pellets were lysed in fractionation buffer (50 mM HEPES pH 7.9, 300 mM NaCl, 0.2 mM EDTA, 0.5% IGEPAL CA-630, 5% glycerol, 1x protease inhibitor). Lysates were centrifuged at 2800 x g for 3 minutes at 4°C and the supernatant was used as soluble fraction. The remaining chromatin pellet was washed once in fractionation buffer before being resuspended in fractionation buffer + 1 mM MgCl2 + 37.5 Units benzonase-nuclease (Millipore). The chromatin pellets were incubated at 37°C for 1 hr shaking at 1000 rpm and frequently resuspended. Then, samples were sonicated for 8 cycles (30s ON, 30s OFF) and the insoluble material was spun down at 17,000 x g for 3 minutes at 4°C. The supernatant was used as chromatin fraction.

Acidic extraction of histones

Cells were harvested using TrypLE, washed once with PBS0 and pellets were incubated in hypotonic buffer (10 mM HEPES pH 7.4, 10 mM KCl, 0.05% IGEPAL CA-630, 1x protease inhibitor) on ice for 10 minutes. Next, samples were spun down at 2000 x g for 5 minutes at 4°C, supernatant was removed and the pellet was washed once with hypotonic buffer. The remaining pellet was incubated in 0.2 M HCl for 45 minutes before being centrifuged at 17,000 x g for 15 minutes at 4°C. The supernatant was used as acidic extracted fraction after being neutralized in neutralization buffer (0.4 M TRIS HCL pH 8, 200 mM NaCl, 10 mM MgCl2, 1x protease inhibitor).

Gel electrophoresis and incubation with antibodies

Cell extracts were run on 4-12% Bolt™ Bis-Tris Plus Mini Protein Gels (Invitrogen) and separated proteins were transferred to a 0.2 μm nitrocellulose membrane (Bio-Rad). After blocking in 5% skimmed milk in PBS, membranes were incubated with primary antibodies in PBS and 1% skimmed milk on a roller overnight at 4°C using the concentrations indicated in the key resources table. For blotting of phospho-proteins, membranes were blocked in 2% BSA (Sigma-Aldrich) and primary antibodies were diluted in PBS and 1% BSA. After incubation with primary antibodies, membranes were washed 3x with PBST and incubated with HRP-conjugated secondary antibody (1:10,000) for 1 hour on a roller at room temperature. Next, membranes were washed 3x with PBST before signal detection using SuperSignal™ West Pico PLUS Chemiluminescent Substrate (ThermoScientific) on the Amersham ImageQuant 800 biomolecular imager.

Flow cytometry

Cells were labeled with EdU (10 μM) for 30 minutes. Subsequently, cells were trypsinized, washed with PBS0 and fixed with 4% paraformaldehyde + 0.1% Triton-X at room temperature (RT) for 15 minutes. Next, cells were washed 2x with FACS buffer (PBS0 + 1% FBS + 0.5 mM EDTA) before being incubated in Click-IT reaction Master Mix (40mM TRIS pH 8, 4 mM CuSO4*5H2O, 10 mM ascorbic acid, 60 μM AF647-Azide) at RT in the dark for 45 minutes. Cells were washed with FACS buffer + 0.1% Triton-X and incubated with primary antibody at RT in the dark for 60 minutes (1/200 for anti-γH2AX, anti-pCHK1 and anti-p21). Samples were washed with FACS buffer and incubated with secondary antibody (1:500 goat-anti-rabbit AF 555) + 1μg/mL DAPI at 4°C O/N rotating. Finally, samples were washed 1x with FACS buffer + 0.1% Triton-X and 2x with FACS buffer. Samples were analyzed on BD LSR Fortessa X20 and results were analyzed using FlowJo™ v10.6.1 Software (BD Life Sciences). To compare DNA replication between conditions, we normalized EdU intensities of S-phase cells by dividing EdU intensities of every cell by the mean of the corresponding G1 population.

Molecular Cell
Article

CellPress
OPEN ACCESS

Repli-ATAC-seq and ATAC-seq
Sample preparation

RPE-1 cells were treated for 2 hours with 1 μM of dTAG (Tocris). For nascent samples, the cells were then pulsed for 20 minutes with 20 μM thymidine analog 5-ethynyl-2′-deoxyuridine (EdU, Abcam) followed by immediate harvest to assess nascent chromatin accessibility. 10x10^5 RPE-1 cells per condition were counted and pooled together with 500 S2 *D.melanogaster* cells to be used for spike-in normalization. The samples were then either de-chromatinized to check for EdU incorporation (controls in Figure S5B), or processed according to the repli-ATAC-seq protocol.[114] Post-replication samples were directly pulsed 20 minutes with 20 μM EdU after which 1 μM of dTAG and 10 μM thymidine were both added for 2 hours (chase) followed by cells harvesting. Mature 2hr and 15hr samples were prepared by treating RPE1 for 2 hours with 1 μM of dTAG, pulse for 20 minutes with 20 μM of EdU and then subjected to a 2- or 15-hours chase with 10 μM thymidine prior harvesting. For the de-chromatinized control samples, after cell harvesting and spike-in addition, were resuspended in 15mM Tris HCl pH 7.5 buffer complemented with 1mM EDTA and 0.5% SDS. These input samples originate from the same tube as the repli-ATAC-seq samples to ensure proper comparison. ProteinaseK (NEB) was added to the cell suspension to a final concentration of 75 μg/ml followed by O.N. incubation on the shaking heat block at 55 C° 1000 rpm. The digested DNA was precipitated with 0.7 volumes of isopropanol and subjected to Tn5 (homemade) digestion after which repli-ATAC-seq samples preparation protocol was followed. Oligos as in Buenrostro et al.[103] were used for library preparation. To prepare classic ATAC-samples, degron-CHAF1A cells were treated with DMSO or 1 μM dTAG for 2 hrs, then 100.000 cells were mixed with 500 EdU-unlabelled *Drosophila* cells. Cell pellet was lysed in 50 μl of ATAC-resuspension buffer 1(ATAC-RSB1 10mM Tris-HCl pH 7.4, 10mM NaCl, 3mM MgCl2, Digitoxin 0.01%, Tween-20 0.1%, IGEPAL CA-630 0.1%) on ice for 3 minutes and wash out with 1 ml of ATAC-RSB2 (10mM Tris-HCl pH 7.4, 10mM NaCl, 3mM MgCl2, Tween-20 0.1%). Nuclei were subjected to Tn5 digestion (TDE1 Illumina kit) for 30 minutes at 37C° in a thermocycler shaking at 1200 rpm. DNA was cleaned up using MinElute Reaction Cleanup kit (Qiagen). Library generation was performed as for repli-ATAC-seq samples, a part from second size selection step where we used a 1.6:1 final ratio of AMPure beads (Beckman Coulter).

Data analysis

Repli-ATAC libraries were sequenced 50 bp pair end modality on Illumina NextSeq2000. Raw, paired-end FASTQ files from repli-ATAC and ATAC protocols were mapped to the human genome (GRCh38, Gencode) and the *Drosophila* genome (dm6, flybase), using the DNA-mapping workflow from snakePipes,[106] with the following command:

DNA-mapping –fastqc –trim –trimmer trimgalore –dedup –mapq 30 –properPairs –insertSizeMax 2000 –alignerOpts ' –very-sensitive' -i <fastq_dir> -o <output_dir> -j 30 <genome>

The workflow applies paired-end trimming using trim-galore (v0.6.5) with options '–paired–stringency 3', maps the reads using bowtie2 (v2.3)[108] with options '–very-sensitive', filters reads with mapq > 30 and insert size < 2000 using samtools (v1.10)[109] and removes PCR duplicates using sambamba (v0.7.1).[110] Further QC and creation of bigwig files was done using deepTools (v3.1).[107]

In order to create spike-in normalized coverage files, we counted the total, de-duplicated reads mapped to the human and *Drosophila* genomes per sample and calculated the size factor (S) per sample as follows.

$$S(x) = \left(\exp \left(\sum \log (x) \right) \Big/ n \right) \Big/ x$$

Where is the counts for spike-in (*Drosophila*) reads per sample, and refers to the number of samples in the same spike-in batch. We used this scale factor to create bigwigs using deepTools bamCoverage and bamCompare, with options '–binSize 15000 –normalizeUsing None –scaleFactor <scalefactor>'. Customed R scripts were used to further analyzed Bam and Bigwig files as well as to analyze all the repli-ATAC and ATAC data (Method S1). We used our ChIC-seq (DMSO control G1 sample) data as a reference to create a merged dataset with information about accessibility and genomic location about H3K9me3 and H3K27me3 heterochromatin region. This new dataset was also overlapped with the VASA-seq data to analyze changes in gene expression in the regions of interest.

scEdU-seq

scEdU-seq was performed as previously described by van den Berg et al.[59] Briefly, RPE-1 cells were labeled with two 15 min pulses of EdU (10 μM) interspersed by 60 minutes washout with full medium. Subsequently, RPE-1 cells were trypsinized and fixed in 70% Ethanol for 24 hours at -20C. Samples were resuspended and washed in Wash Buffer (47.5mL H2O RNAse free, 1ml 1M HEPES pH 7.5, 1.5ml 5M NaCl, 3.6 μl pure spermidine solution with extra 0.05% Tween, 4 μl/ml 0.5M EDTA). Subsequently, Biotin-PEG3-Azide was conjugated to EdU molecules by a CuAAC click reaction and stained with DAPI. Single S-phase RPE-1 hTERT cells were sorted into 384-well plates for scEdU-seq processing. Following the sort, libraries were prepared by the following steps; proteinaseK digestion, NlaIII genome digestion, DNA blunt ending, A-tailing and finally adapter ligation with cell barcodes and unique molecular identifiers (UMI). Single cell libraries were pooled and bound with MyOneC1 Streptavidin beads to capture DNA replication fragments. Fragments were released by heat denaturation and fragments were filled in by the Klenow enzyme. Libraries were amplified by IVT, RT and PCR and subjected to Illumina sequencing (Nextseq1000 P3 2x100bp). Code for analysis and plotting can be found on GitHub https://github.com/jervdberg/CAF1_de_novo_chromatin. Published Repli-Seq[115] and EdU-seqHU[116] data were used as reference for replication timing analysis.

scVASA-seq

scVASA-seq was performed as previously described by Salmen et al.[65] Briefly, total RNA is fragmented and polyadenylated. Total RNA is converted to cDNA and amplified by in vitro transcription. Ribosomal RNA sequences were depleted from Amplified RNA (aRNA) and residual RNA is converted to DNA by reverse transcription. Subsequently, libraries are amplified by PCR and subjected to Illumina sequencing (Nextseq1000 P3 2x100bp). We sequenced the following number of cells per condition: 348 for DMSO-2h, 292 for DMSO-30h, 330 for V1-2h and 353 for V1-30hr. We obtained an average of 61317±1012 reads per cell. Leiden clustering was used to cluster cells, and the expression of the cell cycle genes CDC6, histone H3C3, Ki-67 and cyclin B1 (CCNB1) were used to assign cell cycle stage to the different clusters (Figure S3B). Seurat was used for analyses.[111] The cells and clusters were visualized by UMAP. Nascent transcription in Figure 5F was quantified as follows: spliced reads are defined as reads containing an exon-exon junction. Conversely, unspliced reads contain an intron-exon junction. These unspliced reads are then defined as nascent transcription. In addition, reads that completely fall into either an exon or intron are termed undetermined and are not used for the analysis of Figure 5F. The number of reads per cell split over read classes is: spliced 45423±783, unspliced 7749±96.8, undetermined 8145±138. Code for analysis and plotting can be found on GitHub https://github.com/jervdberg/CAF1_de_novo_chromatin. Gene set lists can be found in Table S1.

ChIC-seq

ChIC-seq (chromatin immunocleavage sequencing) was performed as described previously by Zeller et al.[85] Briefly, cells were treated with DMSO or dTAG for indicated time periods. Subsequently, cells were fixed in 70% Ethanol and within 24 hours resuspended in Wash buffer (47.5ml H2O RNAse free, 1ml 1M HEPES pH 7.5, 1.5ml 5M NaCl, 3.6μl pure spermidine solution, 0.05% Tween, 200μL 0.5M EDTA & Protease inhibitor tablet). Antibodies were incubated overnight at 4°C on a roller to prevent aggregation. After washing away the antibody, pA-MNase was added to the samples in combination with DAPI. Next, a thousand cells were sorted in individual tubes per sample and Ca^{2+} was added to activate the pA-MNase for 30minutes at 4°C, MNase was stopped by the addition of EGTA and digested with proteinase K. The resulting DNA fragments were end-repaired, A-tailed and ligated with double-strand DNA adapters containing a T7 and UMI. Samples were amplified with a round of in vitro transcription, reverse transcriptions and finally PCR. Libraries were subjected to Illumina Sequencing (Nextseq P3 2x100bp). Code for analysis and plotting can be found on GitHub https://github.com/jervdberg/CAF1_de_novo_chromatin.

Microscopy

Live-cell imaging

Cells were plated on a glass bottom 96-well plate (Cellvis Cat. No. P96-1.5H-N) coated with collagen diluted 1:50 in water (Advanced BioMatrix, #5005). Cells were plated at a density of 1,200 cells per well 24hr prior to the start of imaging. For the duration of the movie, cells were maintained in at 37°C, with 5% CO2. Exposure times were set to 70ms for CFP, corresponding to H2B-mTurquoise2 and 100ms for YFP, corresponding to DHB-mVenus. After 24hr of live-cell imaging, cells were treated with either 1μM dTAG-V1 or 0.1% DMSO, followed by an additional 48hr of imaging.

Tracking of live-cell imaging

Live-cell tracking was conducted by generating a nuclear mask based on segmentation of the H2B-mTurquoise fluorescence signal for each frame of the live-cell movie and nearest neighbor calculations were used to track single cells. The nuclear mask was applied to the DHB-mVenus fluorescence channel and the nuclear DHB signal was measured as the mean signal of the pixels in each nucleus. Cytoplasmic DHB signal was determined by dilating the nuclear mask by 2 pixels and calculating the mean pixel intensity of the cytoplasmic ring. CDK2 activity was calculated as the ratio of cytoplasmic to nuclear DHB signal. The tracking code is available at https://github.com/scappell/Cell_tracking.

RNA FISH

Cells were fixed with 4% paraformaldehyde for 15min. Histone H4.2 (Thermo Fisher, VA6-3174283-VC) mRNA was visualized according to the manufacturer's protocol (ViewRNA ISH Cell Assay Kit, Invitrogen QVC0001). Cells were permeabilized for 30min and mRNA probes hybridized for 4hr at 40°C. Exposure time was set to 600ms for Cy5. Histone H4.2 mRNA FISH signal was quantified as the median pixel value of a two-pixel-wide cytoplasmic ring around the nuclear mask.

Quantitative mass spectrometry

Sample preparation for histone modification analysis by MS

Approximately $5 \cdot 10^5$ RPE-1 degron-CHAF1A cells were synchronized in G2 phase as described in Figure 3A and under method section "cell synchronization". Acid extracted histones were processed according to a SP3 protocol as described previously.[117] However, proprietary steps developed by MOLEQLAR Analytics GmbH have been added in order to adjust the protocol for histone specific aspects. Upon overnight digestion at 37°C and 1,000rpm in a table-top thermomixer, samples were acidified by adding 5μl of 5% TFA and quickly vortexed. Beads were immobilized on a magnetic rack, and peptides were recovered by transferring the supernatant to new tubes. Samples were dried down using a vacuum concentrator and reconstituted by adding 12μl 0.1% FA to reach a peptide concentration of approximately 0.2μg/μl. MS injection-ready samples were stored at -20°C.

LC-MS analysis of histone modifications

Approximately 200ng of peptides from each sample were separated on a C18 column (Aurora Elite TS, 15 cm x 75 μm ID, 1.7 μm, IonOpticks) with a gradient from 5% B to 25% B (solvent A 0.1% FA in water, solvent B 100% ACN, 0.1% FA) over 35min at a flow rate of 300nl/min (Vanquish Neo UHPLC-Systems, Thermo Scientific) and directly sprayed into a Exploris 240 mass spectrometer (Thermo-Fisher Scientific). The mass spectrometer was operated in full-scan mode to identify and quantify specific fragment ions of N-terminal peptides of human histone 3.1 and histone 4 proteins. Survey full scan MS spectra (from m/z 250–1600) were acquired with resolution 60,000 at m/z 400 (AGC target of 3x106). Typical mass spectrometric conditions were: spray voltage, 1.9kV; no sheath and auxiliary gas flow; heated capillary temperature, 300°C.

Quantification of histone modifications

Data analysis was performed with Skyline (version 22.2.0.351)[113] by using doubly and triply charged peptide masses for extracted ion chromatograms (XICs). Peaks were selected manually. Heavy arginine-labelled spiketides (13C6; 15N4) were used to confirm the correct retention times. The SILAC peptides (i.e. heavy arginine-labelled peptides (R6 Arginine 13C6)) were selected to assess the newly heavy arginine incorporation into synthetized histones proteins. To that aim, we removed any peptides that did not contain any arginine. Integrated peak values (Total Area MS1) under the first 4 isotopomers were used for further calculations and $\log_2$ transformed. Since the three G1 samples are unlabeled, we used them to evaluate the labeling quality, defined as our ability to not detect hits to peptides containing heavy arginine in G1 condition and measured as the median of 100-100 x intensitySILAC/ (intensitySILAC+intensitylight) percentage over the peptides equal to 98.7, 99.4, and 99.5% for replicates 1, 2, 3 respectively. Subsequently, any SILAC signal in G1 samples was not considered (i.e. set to 0).

For a given precursor, the percentage of each modification on the following H3/H4 lysines: K4, K9, K14, K18, K23 K27, K36, K56, K79/K5, K8, K12, K16 (all denoted as H4_4…17), K20 within the same peptide is derived from the ratio of this structural modified peptide intensity to the sum of all isotopically similar peptides intensities using either SILAC (new) or light intensities (old). In other words, the Total Area MS1 value was used to calculate the relative abundance of an observed modified peptide as percentage of the overall peptide. The intensity of the unmodified peptide of histone 3.1 (aa 41–49) was used as a proxy of total histone 3.1. Coeluting isobaric modifications were quantified using three unique MS2 fragment ions.

Per modification, we tested for any significant difference in differential relative abundance between old and new histones in DMSO versus dTAG condition (i.e. effect of dTAG) using a t test under the following null hypothesis (rel. abund. from light – rel. abund. from SILAC) DMSO = (rel. abund. from light – rel. abund. from SILAC) dTAG. Benjamini-Hochberg multiple-testing procedure has then been applied.

Analysis of senescence-associated β-galactosidase activity

For quantification of SA-β-gal activity by flow cytometry, the CellEvent™ Senescence Green Flow Cytometry Assay Kit (Invitrogen) was used. Cells were treated with either DMSO or dTAG (500 nM) for 7 days without splitting. Next, cells were harvested by trypsinization, washed once with PBS0 and then fixed with 4% paraformaldehyde for 10min at RT. Subsequently, samples were washed with PBS0 and incubated for 2hr in 1:750 CellEventTM Senescence Green Probe diluted in CellEventTM Senescence Buffer at 37°C shaking (1000 rpm). Lastly, cells were washed with PBS0 and analyzed using BD LSR Fortessa X20 (BD Biosciences).

Cell-growth competition assay

RPE-1 mNeonGreen-tagged β-tubulin cells were seeded at a 1:5 ratio with either degron-CHAF1A cells or p53KO degron-CHAF1A cells. Cells were treated with dTAG (500 nM) or DMSO over a period of 7 days and split at day 0, 2 and 4 according to their confluency. The remaining cells of every timepoint were collected for flow cytometry analysis, washed 1x in FACS buffer and the percentage of degron-CHAF1A cells was assessed as mNeon negative population using BD LSR Fortessa X20 (BD Biosciences).

DNA fiber assay

Degron-CHAF1A cells were treated with 500 nM dTAG or DMSO for 2 hr before labelling with 25 μM CldU (Sigma) at 37°C for 20 min. Cells were washed 3x with warm medium before labelling with 250 μM IdU (Sigma) at 37°C for 20 min. Cells were harvested, washed with ice-cold PBS-BSA and fixed in 70% EtOH over-night. Buffer was exchange to cold storage buffer (42.5ml, H2O RNAse free, 5mL DMSO, 1ml 1M HEPES pH 7.5, 1.5ml 5M NaCl, 3.6μl Spermidine, 0.05% Tween, 200μL 0.5M EDTA). Cells were incubated with DAPI in PBS0/BSA (1 μg/mL) for 1 hr and sorted in fractions of early and late S-phase via FACS. Labelled cells ($3 \cdot 10^5$ cells/ml) were lyzed and spread on microscopy slides in lysis/spreading buffer (0.5% SDS, 200 mM Tris pH 7.4, 50 mM EDTA) by slightly tilting the slide. After spreading, the slides were airdried and fixed in 3:1 methanol/acetic acid solution for 10 min. DNA was denatured in 2.5 M HCl for 90 min prior to incubation with rat-anti-BrdU (1:1000; Abcam, cat. no. ab6326) and mouse-anti-BrdU (1:250; BD Biosciences, cat. no. 347580) for 1 hr to label CldU and IdU, respectively. Subsequently, DNA fibers were stained with Alexa Fluor 488-conjugated anti-rat immunoglobulin G (1:500; ThermoFisher; A-11006) and Alexa Fluor 647-conjugated anti-mouse immunoglobulin G (1:500; ThermoFisher; A32728) for 90 min. Lastly, DNA fibers were imaged on the Zeiss Axio Imager Z2 and fiber lengths were measured in FIJI.[112] Per condition, three replicates were measured, with 100 fibers analyzed per replicate.

Molecular Cell
Article

QUANTIFICATION AND STATISTICAL ANALYSIS

Quantification and statistical analyses are described in the figure legends and STAR Methods sections. R and GraphPad Prism 9 were used for calculations. The pairwise t test and corrected Bonferroni multiple testing was used for scEdU-seq and scVASA-seq data. Comparison between different regions in repli-ATAC-seq data was quantified using one-way ANOVA test and Wilcoxon-Test. P-values in SILAC data in Figures 4E and S4G are measured using the Benjamini-Hochberg adjustment. In the other cases, t tests are used and specified in the legends. In all cases, statistical significance was defined as follows: ns (not significant), $p > 0.05$, $*p < 0.05$, $**p < 0.01$, $***p < 0.001$, $**** < 0.0001$. Error bars represent standard deviation (SD).